J. Fluid Mech. (2007), *vol.* 582, *pp.* 281–318.
doi:10.1017/S0022112007005836 Printed in the United Kingdom

Direct numerical simulation of stenotic flows. Part 2. Pulsatile flow

SONU S. VARGHESE[1], STEVEN H. FRANKEL[1]
AND PAUL F. FISCHER[2]

[1]School of Mechanical Engineering, Purdue University, 585 Purdue Mall, West Lafayette, IN 47907, USA

[2]Mathematics and Computer Science Division, Argonne National Laboratory, Argonne, IL 60439, USA

(Received 29 January 2005 and in revised form 16 January 2007)

Direct numerical simulations (DNS) of stenotic flows under conditions of steady inlet flow were discussed in Part 1 of this study. DNS of pulsatile flow through the 75 % stenosed tube (by area) employed for the computations in Part 1 is examined here. Analogous to the steady flow results, DNS predicts a laminar post-stenotic flow field in the case of pulsatile flow through the axisymmetric stenosis model, in contrast to previous experiments, in which intermittent disturbed flow regions and turbulent breakdown were observed in the downstream region. The introduction of a stenosis eccentricity, that was 5 % of the main vessel diameter at the throat, resulted in periodic, localized transition to turbulence. Analysis in this study indicates that the early and mid-acceleration phases of the time period cycle were relatively stable, with no turbulent activity in the post-stenotic region. However, towards the end of acceleration, the starting vortex, formed earlier as the fluid accelerated through the stenosis at the beginning of acceleration, started to break up into elongated streamwise structures. These streamwise vortices broke down at peak flow, forming a turbulent spot in the post-stenotic region. In the early part of deceleration there was intense turbulent activity within this spot. Past the mid-deceleration phase, through to minimum flow, the inlet flow lost its momentum and the flow field began to relaminarize. The start of acceleration in the following cycle saw a recurrence of the entire process of a starting structure undergoing turbulent breakdown and subsequent relaminarization of the post-stenotic flow field. Peak wall shear stress (WSS) levels occurred at the stenosis throat, with the rest of the vessel experiencing much lower levels. Turbulent breakdown at peak flow resulted in a sharp amplification of instantaneous WSS magnitudes across the region corresponding to the turbulent spot, accompanied by large axial and circumferential fluctuations, even while ensemble-averaged axial shear stresses remained mostly low and negative. WSS levels dropped rapidly after the mid-deceleration phase, when the relaminarization process took over, and were almost identical to laminar, axisymmetric shear levels through most of the acceleration phase.

1. Introduction

Part 1 (Varghese, Frankel & Fischer 2007) of this study dealt with steady flow through both axisymmetric and eccentric stenosis models, with the geometry and flow conditions selected to match the classic stenotic flow experiments of Ahmed & Giddens (1983). For the range of Reynolds numbers considered, the numerical simulations under steady inlet conditions predicted laminar flow in the case of the axisymmetric

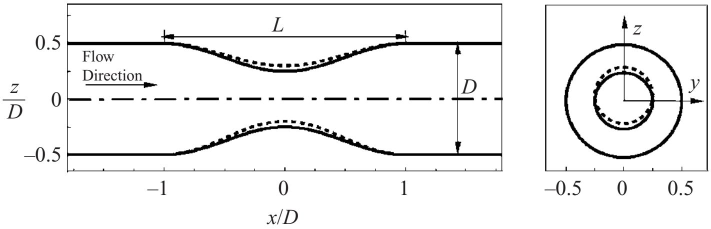

FIGURE 1. Side and front views of the stenosis geometry ($L = 2D$), the solid line corresponding to the profile of the axisymmetric model and the dashed line to the eccentric model; x is the streamwise direction while y and z are the cross-stream directions. The front view shows the cross-section corresponding to both models in the main vessel and at the throat, $x = 0$.

model, with no disturbances downstream of the stenosis throat (neck). In contrast, the introduction of a small eccentricity within the stenosis, 5 % of the main vessel diameter at the throat, resulted in localized transition to turbulence in the region beyond six vessel diameters downstream of the throat for the highest Reynolds number considered. The nature of the turbulence was found to closely resemble localized structures observed during pipe flow transition at similar Reynolds numbers. As a result of turbulent breakdown, large spatial variations of wall shear stress were observed along the post-stenotic walls.

The steady flow results provide an insight into the complexities that may arise in the presence of a stenosis, especially one that is asymmetric, and serve as a precursor to more physiologically realistic pulsatile flow simulations. The complex flow features seen in the steady flow case, involving flow separation, recirculation, reattachment, and strong shear layers, when combined with flow pulsatility, can result in periodic transition to turbulence downstream of the stenosis. This paper discusses pulsatile flow results obtained by using the same stenosis models as used in Part 1 for the steady flow simulations, under flow conditions matching those of Ahmed & Giddens (1984). The goal is to study post-stenotic transition to turbulence in the presence of stenosis asymmetry, complementing earlier stenotic flow studies and providing a fundamental basis for understanding the flow dynamics that influence variables such as wall shear stress, which have been found to play a role in the progression of arterial disease (Ku 1997). The asymmetry is especially relevant from the physiological perspective since real-life arterial stenoses are unlikely to be perfectly symmetric (Stroud, Berger & Saloner 2000).

The spectral-element code employed here was designed specifically for simulating transitional flows in complex geometries (Fischer, Kruse & Loth 2002); details on the numerical methodology are given in Part 1. The flow model and data reduction procedure are outlined in § 2. As in Part 1, comparisons with experiments are included in the results and discussion presented in § 3. Conclusions follow in § 4.

2. Problem formulation

2.1. *Flow model and dimensionless groups*

The axisymmetric and eccentric stenosis geometries modelled in this study were similar to those introduced in Part 1, matching the models employed in the stenotic flow experiments of Ahmed & Giddens (1983, 1984). The stenosis axis was offset by $0.05D$, D being the vessel diameter, in the eccentric model. Profiles of the axisymmetric and eccentric models are shown in figure 1 for ease of reference. For the pulsatile flow simulations reported in this paper, the Womersley solution (Womersley 1955) for laminar, pulsatile flow through rigid tubes was used as the inlet boundary condition, specified as

$$\left.\begin{aligned} \frac{u}{u_c} &= [1-r^2] + A\left[\frac{1-J_0\left(i^{3/2}\alpha 2r/D\right)}{J_0\left(i^{3/2}\alpha\right)}\right]\sin(\omega t), \\ \frac{v}{u_c} &= 0, \\ \frac{w}{u_c} &= 0, \end{aligned}\right\} \tag{2.1}$$

where u, v and w are velocity components in the x-, y- and z-directions, respectively, u_c is the mean (cycle-averaged) centreline inlet velocity, A is the amplitude of pulsation, $J_0()$ is the Bessel function of type 0, ω is the angular frequency of pulsation, and α is the non-dimensional Womersley parameter $(=\frac{1}{2}D\sqrt{\omega/\nu}$, with ν being the kinematic viscosity). The Reynolds and Womersley numbers are both ratios of inertial and viscous forces, with the former dealing with steady inertia (sometimes defined instantaneously) while the latter deals with purely oscillatory inertia and is properly defined only for pipe flows. The Womersley parameter essentially defines the extent to which the laminar profile departs from quasi-steadiness, an effect that becomes significant by $\alpha = 3$.

In both the axisymmetric and eccentric models, the upstream and downstream sections of the vessel extended for 3 and 16 vessel diameters, respectively, as measured from the stenosis throat. Rigid vessel walls were assumed throughout, with the no-slip condition applied at them. The outflow boundary condition treatment discussed in Part 1 was employed for the current simulations as well, effectively adding a constant to the outward normal component of the velocity field to ensure that the characteristics are always pointing outwards. The effect of this treatment was confirmed to be restricted to the outflow region, $x > 14D$, for all the cases reported here.

All parameters and normalizations employed in this study were chosen to replicate the flow conditions in the experiments by Ahmed & Giddens (1984) to facilitate comparison with their measurements. The Reynolds number based on the main vessel diameter, D, and mean inlet centreline velocity, u_c, was 600, with minimum and maximum Reynolds numbers of approximately 200 and 1000, respectively, corresponding to a value of $A = 0.667$ in equation (2.1). The Womersley number, α, was chosen as 7.5. The velocity waveform at the inlet was sinusoidal, as the boundary condition in equation (2.1) defines, and the resulting inlet centreline velocity is shown in figure 2. Results presented in the following sections were obtained at intervals of $T/6$ (T being the period of pulsation). The six phases in the pulsatile cycle, indicated in figure 2, were deemed sufficient to accurately represent the temporal evolution of the flow.

2.2. *Data reduction*

In unsteady flows, similar to the pulsatile flow cases studied here, several types of averaging operations can be employed. For a generic flow variable f, the time-averaged mean over a period of time T_f is computed as

$$\overline{f}(x,y,z) = \frac{1}{T_f}\int_{t_0}^{t_0+T_f} f(x,y,z,t)\,\mathrm{d}t, \tag{2.2}$$

where t_0 is the time at which the averaging process is initiated. The deviation from this average, which represents random turbulent fluctuations, is then defined as

$$f'(x,y,z,t) = f(x,y,z,t) - \overline{f}(x,y,z). \tag{2.3}$$

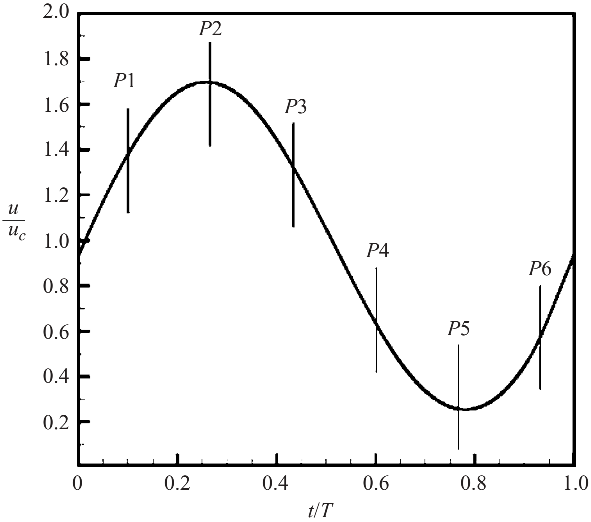

FIGURE 2. Axial centreline velocity at the vessel inlet. Reference phases at which results are presented are also indicated.

The time-averaging operation defined in equation (2.2) is typically employed to analyse steady flow data, as in Part 1. In the case of pulsatile flow, $T_f = NT$, where N is the number of time-period cycles over which time integration is performed and T is the time period of each pulsatile cycle. Additionally, an ensemble-averaging operator that represents the time-varying coherent response to the pulsatility (Lieber & Giddens 1988; Scotti & Piomelli 2001; Mittal, Simmons & Najjar 2003) can be defined over N time-period cycles as

$$\langle f \rangle(x, y, z, t) = \frac{1}{N} \sum_{n=0}^{N-1} f(x, y, z, t + nT). \tag{2.4}$$

In order to distinguish between the scales associated with pulsation and those from random turbulent motions, the fluctuation with respect to the phase average, differentiated from the time-average fluctuation in equation (2.3) by using a double prime, is defined as

$$f''(x, y, z, t) = f(x, y, z, t) - \langle f \rangle(x, y, z, t). \tag{2.5}$$

The root mean square (r.m.s.) quantities are computed as

$$f''_{rms} = \sqrt{\langle f''^2 \rangle}. \tag{2.6}$$

2.3. *Grid resolution and simulation details*

Simulation of pulsatile flow through the axisymmetric stenosis was conducted with a polynomial order of $N = 8$ on a mesh comprising $K = 1600$ hexahedral cells (≈820 000 grid points). N and K are defined in Part 1 of this study. The mesh was found to be adequate for this case by comparing results to those obtained on a mesh with $N = 11$ (≈2.13 million grid points). The corresponding eccentric model simulations were conducted with $N = 11$ on a mesh with $K = 2400$ cells (≈3.2 million grid points) to obtain sufficient resolution for the turbulent case. Grid independence was confirmed by increasing the polynomial order to $N = 13$ (≈5.27 million grid points) and comparing results. Axial velocity profiles obtained using the two different meshes are shown in

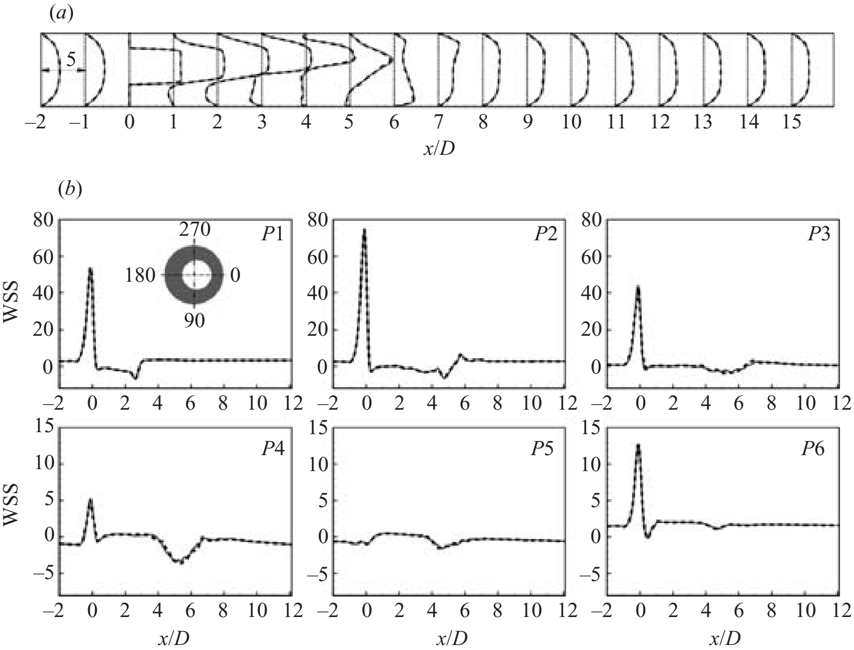

FIGURE 3. Resolution studies for pulsatile flow through the 75 % eccentric stenosis. Results were obtained on two meshes, corresponding to $K = 2400$, $N = 11$ (dashed line) and $K = 2400$, $N = 13$ (solid line). (*a*) Comparison of ensemble-averaged axial velocity profiles, u/u_c, during peak inlet flow conditions. (*b*) Comparison of axial wall shear stress (WSS) during phases $P1 - P6$. WSS has been averaged over the four circumferential locations indicated.

figure 3(*a*) and indicate excellent agreement. These profiles were obtained under peak inlet flow conditions when turbulent breakdown occurred and were ensemble-averaged over twenty-five cycles. Figure 3(*b*), which shows ensemble-averaged axial wall shear stress (WSS) for the two meshes, averaged over the four circumferential locations indicated in the figure, further demonstrates that the resolution is satisfactory. Physical interpretation of the velocity and WSS profiles is postponed until § 3.2. Turbulent statistics presented in the results section were all obtained on the $K = 2400$, $N = 13$ mesh.

The axisymmetric model simulation was initiated from steady flow results obtained at $Re = 500$, presented in Part 1, while the eccentric model employed results from the axisymmetric case as the initial condition. Results presented for the axisymmetric model were obtained following four initial cycles from the start, by which time the flow was found to have reached a periodic state. Twelve initial cycles were run for the eccentric model. In both cases, the velocity at 120 axial locations along the vessel were monitored and plots of the instantaneous axial velocity at these locations versus time, as in figure 4(*a*), were used to ensure time periodicity of the flow within visual limits and that initial transients had left the computational domain. In addition to these, ensemble-averaged and r.m.s. quantities (as defined in § 2.2) were continuously monitored. Figure 4(*b*) shows a log plot of cross-stream r.m.s. velocity, w_{rms}/u_c, at four locations along the vessel centreline during the initial twelve cycles of simulation. The r.m.s. velocity can be observed to have reached a time-periodic state by this time.

For the eccentric model, ensemble-averaged statistics, as defined in § 2.2, were collected over the final 25 time period cycles, following the initial 12 cycles. Using 25 cycles reduces non-coherent activity by a factor of 5 but does not completely

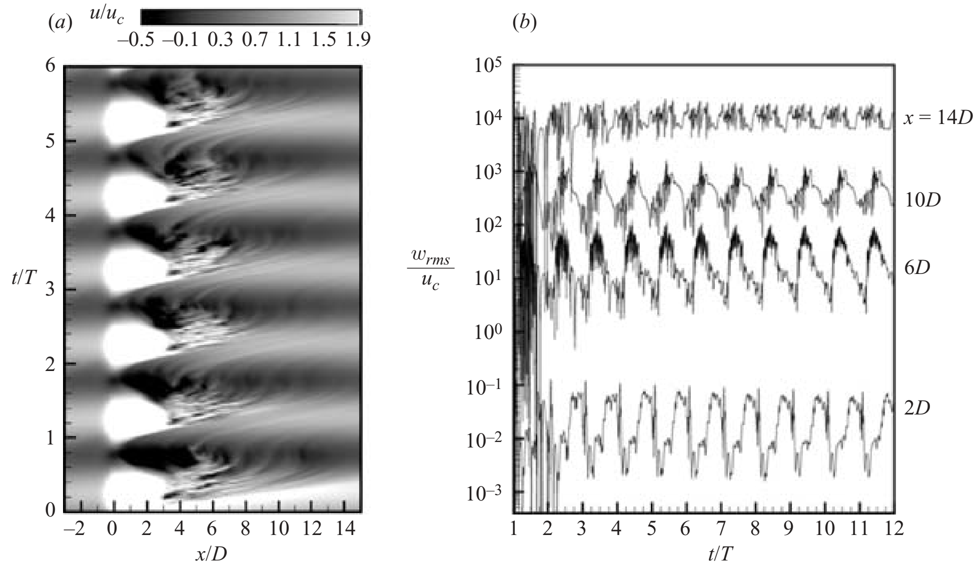

FIGURE 4. (*a*) Contours of instantaneous centreline axial velocity, u/u_c, during the first six time period cycles for simulation of pulsatile flow through the 75 % eccentric stenosis. (*b*) Log plot of cross-stream r.m.s. velocity, w_{rms}/u_c, versus time at four axial stations along the vessel centreline, computed during the first 12 cycles of simulation (the first cycle has been omitted). The r.m.s. velocity at each axial station is offset by 100 log units.

eliminate it. The number of cycles was limited by computational and storage constraints, with large quantities of data ($\approx$ 50 gigabytes) being generated per cycle. This is however in line with the 10 to 25 cycles used by Ahmed & Giddens (1984) and the 20 cycles used by Lieber & Giddens (1990) to construct ensemble-averages in their pulsatile stenotic flow experiments. More recently, Mittal *et al.* (2003) employed eight cycles to compute statistics and frequency spectra for their large-eddy simulations (LES) of pulsatile flow in a constricted channel while Sherwin & Blackburn (2005) used 10 cycles in their stability analysis studies of axisymmetric stenotic flows.

A non-dimensional time-step size of 1.0×10^{-3} was used for simulating pulsatile flow through the axisymmetric stenosed vessel but this had to be lowered to 2.5×10^{-4} for the eccentric model, in which flow transitioned to turbulence, and consequently, this case was the most computationally challenging simulation. The time-step sizes are for the highest resolution meshes in both cases. Simulation of one time period cycle through the axisymmetric model ($K = 1600$, $N = 11$ mesh) required less than four wall-clock hours on 256 processors of the IBM BGL machine at Argonne National Laboratory. The eccentric model simulations were run on up to 1024 processors of the same machine and on the $K = 2400$, $N = 13$ mesh, computing time for one time period cycle was close to ten wall-clock hours.

3. Results and discussion

3.1. *Axisymmetric model*

Figures 5 and 6, respectively, show axial velocity profiles and vorticity magnitude contours from the simulation of pulsatile flow through the axisymmetric stenosis. The velocity profiles upstream of the stenosis correspond to the Womersley solution as defined in equation (2.1). Past the mid-acceleration phase ($P1$), the flow upstream

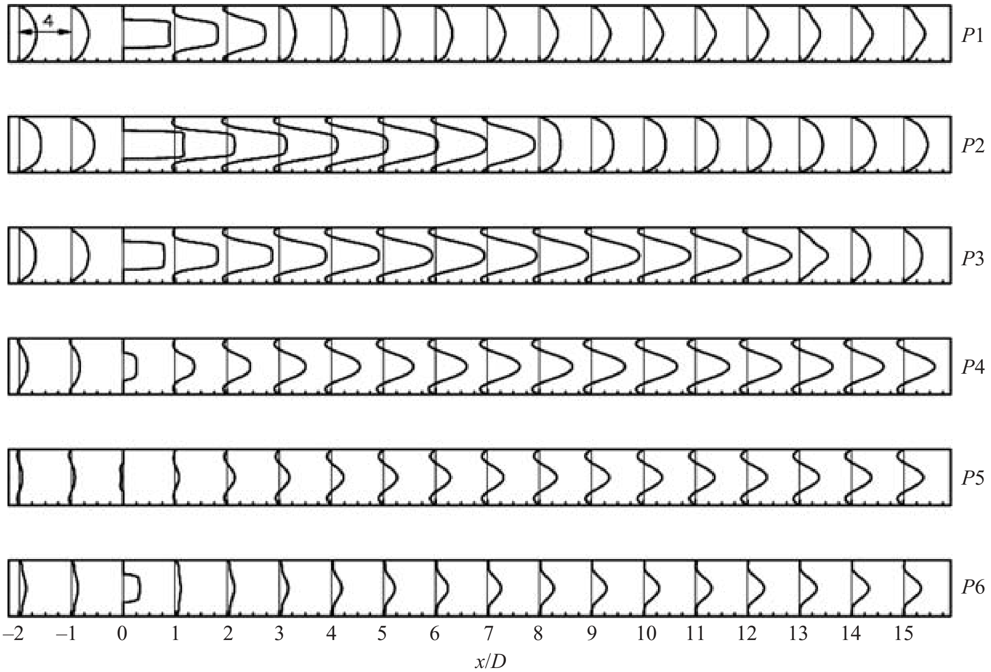

FIGURE 5. Sequence of axial velocity profiles, u/u_c, for pulsatile flow through the 75 % axisymmetric stenosis.

almost resembles the parabolic profile seen in fully developed steady pipe flow. The upstream centreline velocity is almost 1.5 times the mean inlet centreline velocity (u_c) at this point. As in the steady flow case, the flow rapidly accelerates through the stenosis creating a plug-shaped profile at the throat with peak velocities greater than $3.5u_c$. The stenotic jet and separation region that form immediately downstream of the stenosis extend past the $x = 2D$ axial station, even as the flow field in the spatial region beyond $x = 3D$ is still recovering from the activity of the stenotic jet that traversed the post-stenotic section during the previous cycle. The corresponding sequence of vorticity magnitude contours in figure 6 shows the vortex ring at the front of the jet propagating downstream over the course of the cycle, followed by a trail of vorticity that extends back to the stenosis throat, where the shear layer was first created. At phase $P1$, the vortex ring is located between $x = 2D$ and $3D$.

The vortex ring moves past the $x = 7D$ station during phase $P2$, when maximum flow conditions exist at the inlet, indicating that the vortex travelled about five vessel diameters within a time span of $T/6$. As the inlet flow reaches peak acceleration, peak velocities at the throat rise above $4.5u_c$, and the centreline velocity at the jet front is greater than $3.5u_c$. In spite of subsequent flow deceleration at the inlet, the results show that the jet continues to propagate downstream over the $T/6$ interval following peak flow, with the vortex ring and separation zone moving past the $x = 12D$ axial station during early deceleration ($P3$). At this phase, the peak jet velocity drops to about $3.0u_c$ and $3.5u_c$ at the throat and jet front, respectively. As deceleration continues past the halfway point, the trailing shear layer at the stenosis throat dies away, and the vortex ring is convected out of the domain at least $T/4$ before the inlet flow reaches a minimum. Flow separation extends over the entire post-stenotic section during the late stage of deceleration ($P4$). At the same time, the adverse

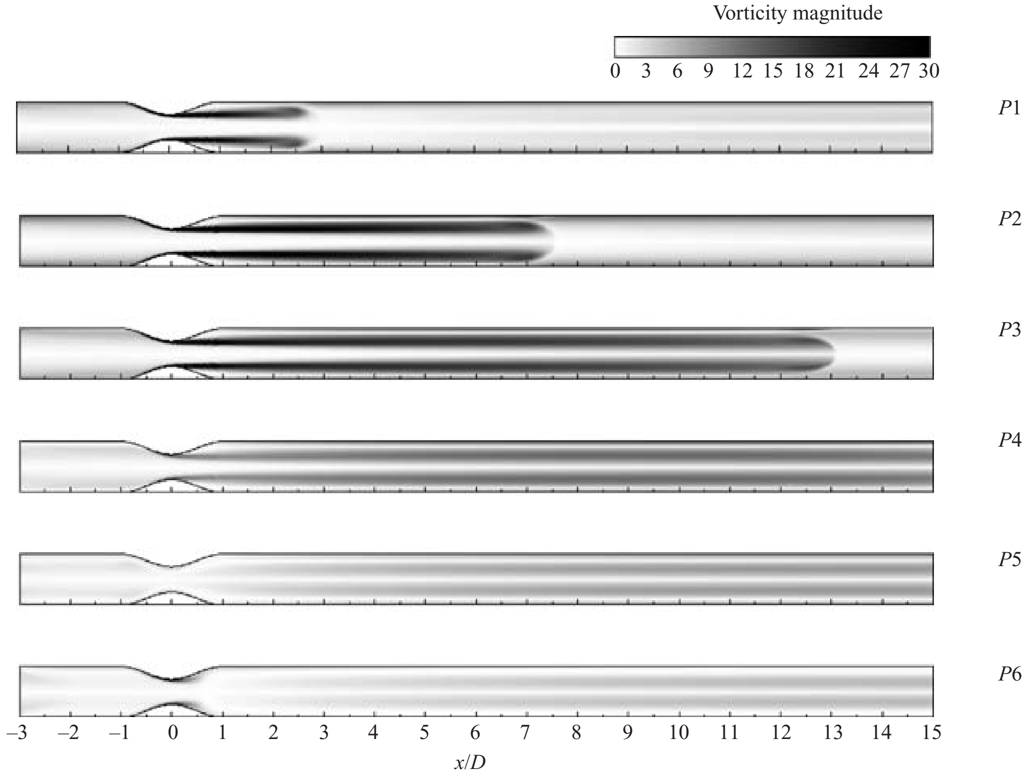

FIGURE 6. Sequence of vorticity magnitude contours, normalized by u_c/D, for pulsatile flow through the 75 % axisymmetric stenosis.

pressure gradient during this phase results in the formation of a small separation region upstream of the stenosis, as evidenced by the profiles at $x = -1D$ and $-2D$.

Flow separation in the upstream section continues through the cycle until minimum inlet flow conditions ($P5$), with upstream centreline velocities dropping to less than $0.3u_c$ by this time. The adverse pressure gradient at this point in the cycle is large enough to create a small flow reversal region at the stenosis throat, due to which the shear layer completely detaches itself from the stenosis. As the pressure gradient once again becomes favourable in the early part of the acceleration phase, the flow starts to accelerate again, and the beginnings of a new jet can be seen forming during the early acceleration phase $P6$. A new shear layer starts to form at the lip of the stenosis, even as the shear layer created during the previous cycle continues to lose its strength and is eventually pushed out of the domain. The velocity profiles also indicate that the flow has completely reattached to the wall, both upstream and downstream of the stenosis, by $P6$. There is no permanent recirculation region in the downstream flow field, in contrast to the post-stenotic flow field observed under steady inlet conditions.

Computed axial velocity profiles during peak inlet flow conditions ($P2$) are compared with experimental measurements by Ahmed & Giddens (1984) in figure 7. As in the steady flow axisymmetric model, profiles computed downstream of a 73 % stenotic occlusion are also included in the comparisons. The results predicted for the 73 % model are in better agreement with the experiments at locations close to the stenosis, similar to the comparisons made for the steady flow case in Part 1. Only at $x = 4D$ and $6D$ is there a small disagreement between the profiles, especially in the

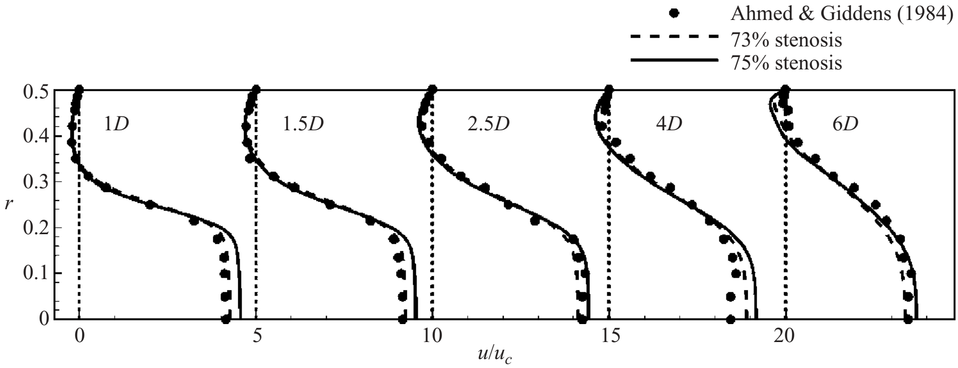

FIGURE 7. Comparison of axial velocity profiles at downstream locations with experimental profiles for pulsatile flow through the axisymmetric stenosis, under conditions of peak flow at the inlet. The axial stations are indicated in terms of diameters downstream from the stenosis throat.

near-wall region, with flow appearing to reattach a little earlier in the experiments. These differences, which are less than 5 %, are smaller than those observed under steady flow conditions, where differences were between 15 % and 20 % in the vicinity of the experimental reattachment location. Experimental measurements downstream of $x = 6D$ were not available.

3.2. *Eccentric model – transition to turbulence*

Under similar flow conditions (the same Reynolds and Womersley numbers) to those used for the axisymmetric model described in the previous section, the introduction of a geometric perturbation, in the form of a $0.05D$ eccentricity at the stenosis throat, causes the flow to deviate markedly from axisymmetry. The pulsatility contributes to periodic localized transition to turbulence during the deceleration phase and subsequent relaminarization during the acceleration part of the cycle, as will be detailed in this section. The statistics presented here were obtained by averaging over 25 time period cycles. As discussed earlier, this reduces non-coherent activity only by a factor of 5 and does not completely eliminate it.

3.2.1. *Evolution of averaged flow characteristics*

Figures 8 and 9 show ensemble-averaged axial velocity profiles and vorticity magnitude contours, respectively, in both the vessel bisecting planes. The results obtained along the two planes considered illustrate the spatial evolution of the flow throughout the pulsatile cycle and the breaking of axisymmetry in the downstream flow field as a result of the eccentricity. During phase $P1$, the velocity and vorticity plots in the plane of eccentricity ($y = 0$) show the plug-shaped jet, formed as the flow accelerates through the constriction, being deflected toward the side of the eccentricity. The velocity profiles in both planes of interest reveal the extent of the resulting asymmetric recirculation zone that forms immediately downstream of the stenosis. In keeping with the spatial evolution of flow observed for the axisymmetric case, the jet and accompanying flow separation zones along the walls extend only past the $x = 2D$ station at this stage, beyond which the flow continues to recover from the activity of the previous cycle. In fact, the profiles indicate that the flow in the far downstream section has not yet regained its upstream character by this late stage of acceleration, even though it achieves axisymmetry after $x \approx 9D$. Some evidence of shear layer roll-up at the front of the jet can be seen in the vorticity results along the $y = 0$

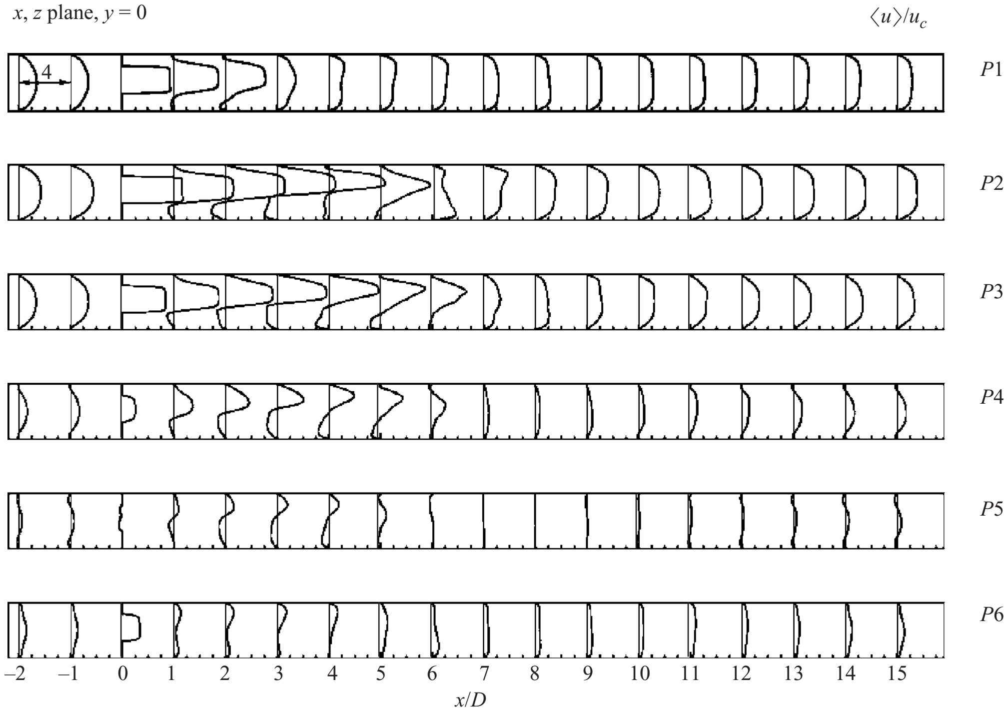

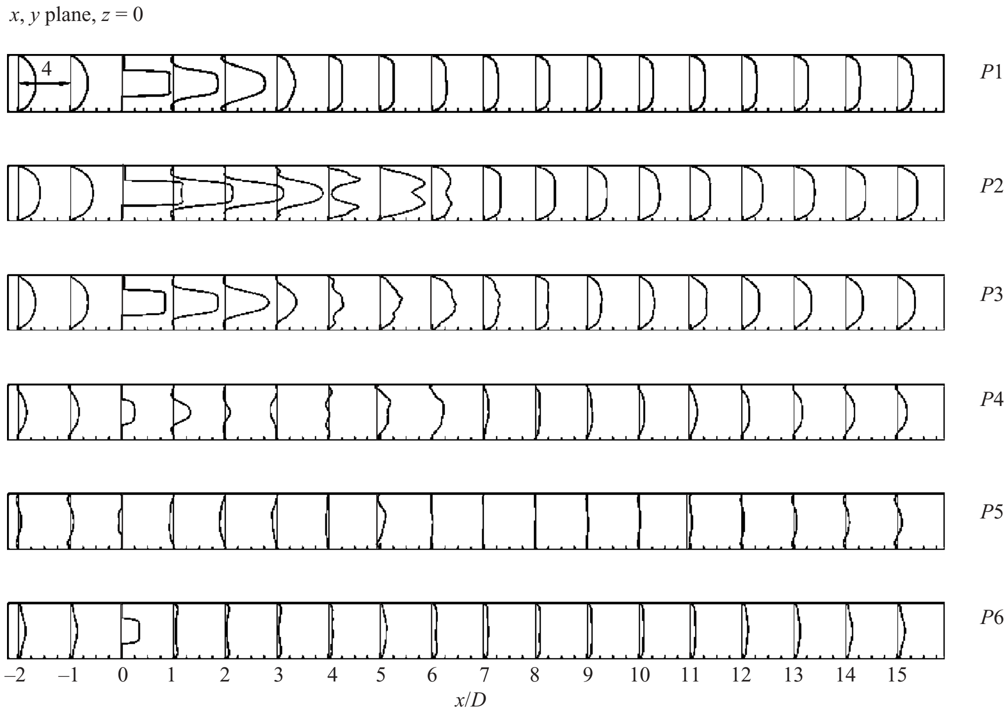

FIGURE 8. Sequence of ensemble-averaged axial velocity profiles, $\langle u \rangle / u_c$, for pulsatile flow through the 75 % eccentric stenosis.

plane. This is reminiscent of the Kelvin–Helmholtz instability typically seen in free shear flows and indicates that the shear layer becomes increasingly unstable toward the end of acceleration, a manifestation of the highly inflected velocity profiles in this region.

The vorticity magnitude contours in figure 9 show that with the reversal of the pressure gradient under peak inlet flow, at phase $P2$, the jet and shear layer break down as they are deflected away from the wall at $x \approx 4D$; the flow apparently undergoing transition to turbulence subsequently, between $x = 4D$ and $6D$. The increased mixing in this region as a result of the unstable jet unsuccessfully attempting to negotiate the wall boundary constraint leads to complete flow reattachment by $x = 6D$. The velocity profiles in the turbulent region, $x = 5D$ to $7D$, start to lose their jet-like character and tend toward uniformity, unlike the continuing jet-like characteristics of corresponding velocity profiles obtained during peak flow conditions for the axisymmetric case, shown in figure 5.

Turbulent jet breakdown continues into the early half of the deceleration phase, dominating the post-stenotic region between $x = 4D$ and $7D$. In the axisymmetric model, flow separation extended as far as $x = 12D$ during phase $P3$, whereas in the eccentric model, separation is present only till $x \approx 6D$, beyond which the velocity profiles resemble the uniform profiles common to turbulent flows. The flow field in the far downstream region is laminar, with the profiles in both planes regaining their upstream character after $x \approx 11D$.

The flow separation region that was formed immediately downstream of the stenosis toward the end of the acceleration phase is present throughout the deceleration part of the cycle. However, the reattachment point stays stationary, lying between $x = 6D$ and $7D$, unlike the axisymmetric case in which the reattachment point moved farther downstream as deceleration progressed. Past the mid-deceleration point, viscous effects start to dominate the flow field, and the shear layer begins to weaken. The inlet flow rate reduces considerably during the late stages of deceleration and the recirculation regions start to recede at phase $P4$. The shear layer eventually detaches itself from the stenosis lip at minimum inlet flow conditions.

The velocity profiles in the region beyond $x > 7D$ during the late stages of deceleration and even minimum flow, $P4$ and $P5$ respectively, illustrate that the turbulent activity that occurred earlier in the cycle completely destroys any effect of the stenosis on the flow field in the far downstream region. This is in sharp contrast to the jet-like character of the profiles predicted for the axisymmetric case close to the outflow boundary. In the eccentric case, throughout the deceleration phase, figure 8 shows that for $x > 11D$ the profiles in both planes closely resemble their upstream counterparts, indicating that the flow has completely relaminarized and regained its axisymmetry this far downstream of the stenosis. This situation occurs even in the early acceleration phase $P6$, which once again sees the formation of a new jet and shear layer as the flow rate increases. Forward flow exists across the entire vessel during these initial stages of the cycle when a favourable pressure gradient exists, with post-stenotic separation zones created only as the flow rate passes the halfway point of acceleration.

3.2.2. *Unsteady recirculation regions*

A closer look at the behaviour of the recirculation regions is worthwhile because these directly correspond to locations of low wall shear stress along the post-stenotic vessel walls, a factor than has been implicated in atherosclerotic disease progression. The effect of the eccentricity in this regard is critical in that the size of the recirculation

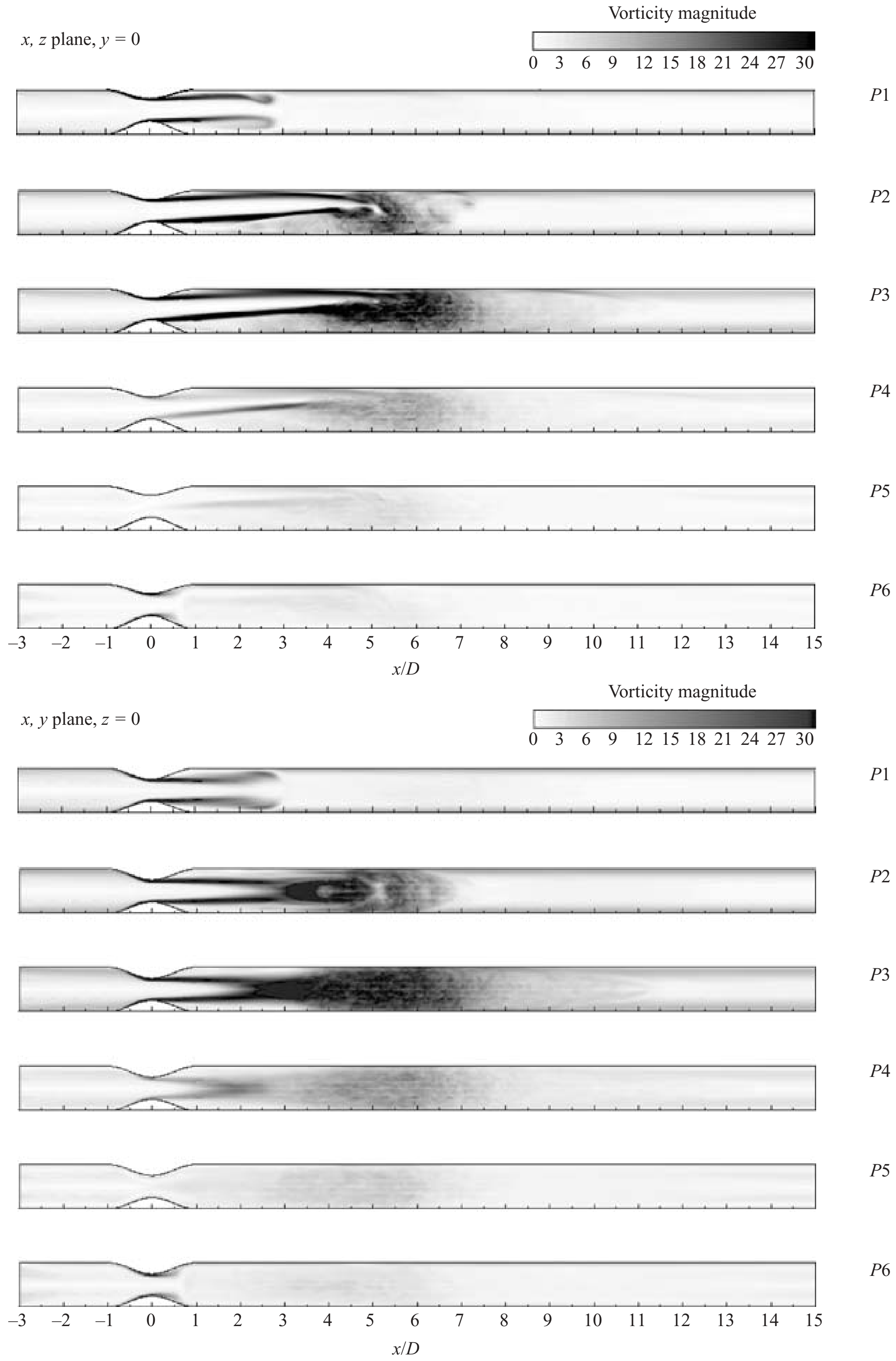

FIGURE 9. Sequence of ensemble-averaged vorticity magnitude contours, normalized by u_c/D, for pulsatile flow through the 75 % eccentric stenosis.

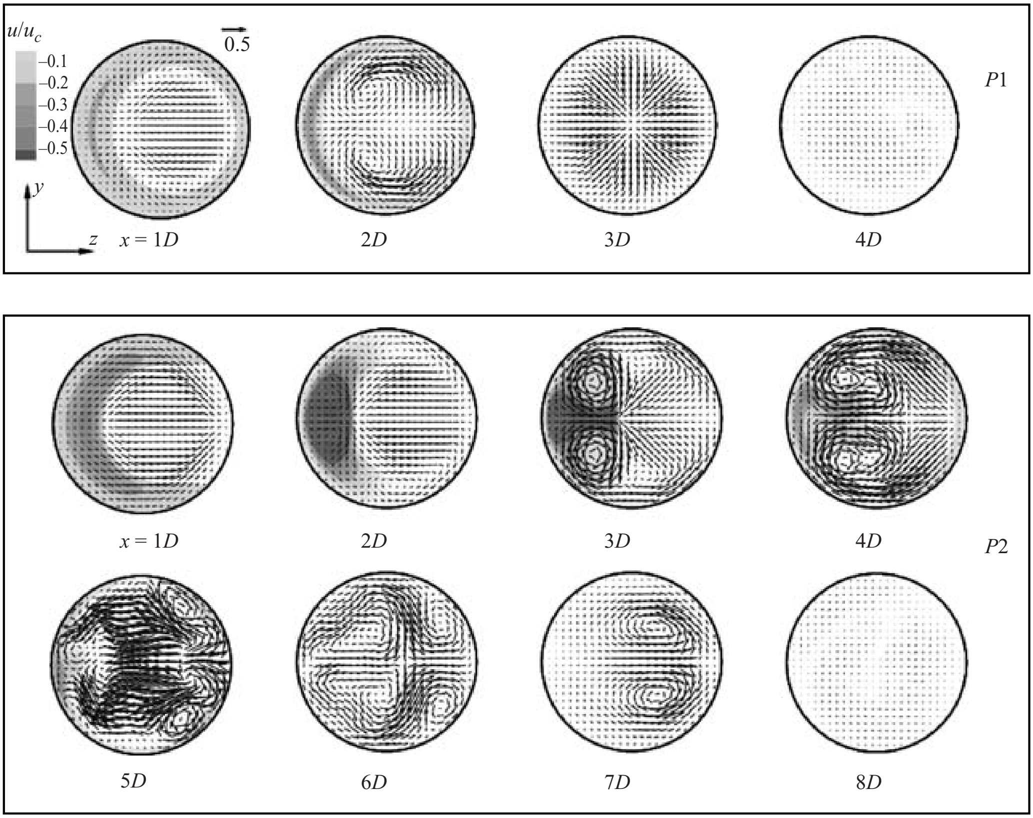

FIGURE 10. Ensemble-averaged velocity results during the late acceleration phase and peak flow, for pulsatile flow through the 75 % eccentric stenosis. In-plane velocity vectors are superimposed on axial velocity contours at downstream stations. Axial velocity levels above 0 have been blanked out to highlight reverse flow regions. All three components of velocity have been normalized by u_c.

regions downstream of the stenosis is significantly larger than the size of those observed in the post-stenotic region of the axisymmetric stenosis model. Figures 10 and 11 show ensemble-averaged, in-plane velocity vectors superimposed on axial velocity contours during the acceleration and deceleration stages of the pulsatile cycle, respectively. Reverse flow regions have been highlighted by blanking out positive axial flow regions.

In figure 10, an asymmetric flow separation region can be seen to form immediately downstream of the stenosis during phase $P1$, as the flow picks up momentum past the halfway point of acceleration and fluid accelerates through the throat. The eccentricity results in a recirculation region forming along the side of the vessel opposite the side that is in closer proximity to the stenosis, and toward which the jet is initially deflected. At this stage, the front of the stenotic jet at $x \approx 3D$ appears relatively undisturbed, with cross-stream velocities directing fluid toward the low-pressure region created by the jet at the vessel core. The downstream recirculation zone grows rapidly toward the end of acceleration; at peak flow ($P2$), an intense reverse flow region forms between $x = 2D$ and $3D$, even as cross-stream velocities larger than $0.5u_c$ after the latter axial station serve to reduce the size of these regions by entraining more fluid into them. As a result of jet breakdown and increased mixing in the region $x > 3D$, as the large in-plane velocity vectors ($> 0.5u_c$ at $x = 4D$ and $5D$) indicate, complete flow reattachment occurs by $x \approx 6D$. This is almost two vessel diameters earlier than in the axisymmetric model at $P2$. The profiles in the $y = 0$ plane also show that the point of maximum reverse flow, which is 100 % of u_c at $x = 3D$ moves closer to the walls with increasing axial distance from the throat, while at the same time dropping in magnitude.

Figure 11 shows the core of the recirculation zone moving farther downstream and closer to the walls throughout the deceleration phase, even as this region attains its maximum cross-sectional extent around $x = 4D$ during this stage of the cycle. The profiles in figure 8 confirm that maximum reverse flow levels, greater than 100 % of u_c, occur between $x = 3D$ and $5D$ during phase $P3$. In-plane velocity vectors in figure 11 indicate that during this phase, cross-stream velocities are of the order of $0.5u_c$ in the breakdown region between $x = 4D$ and $6D$. Figure 11 shows a significant reduction in size of the recirculation zone toward the end of deceleration, from phase $P4$ through to $P5$, occupying only a small area of the vessel cross-section during the latter phase (minimum flow). It disappears completely during the early stages of acceleration, confirming that a permanent recirculation zone is absent, as in the axisymmetric model.

We note that ensemble-averaged flow characteristics such as the results in figures 8, 10 and 11 serve only to highlight post-stenotic reverse flow activity and may not reveal the precise unsteady nature of the flow in the recirculation regions; instantaneous snapshots are required to obtain a clearer picture.

3.2.3. *Temporal evolution*

Figure 12(*a*) shows the time history of instantaneous axial velocity at several axial stations along the centreline of the vessel, featuring flow disturbances as they appear downstream of the stenosis with each new cycle. Only 10 out of the 25 cycles used for ensemble-averaging are shown. The corresponding ensemble-averaged velocity waveforms in figure 12(*b*), albeit a rough estimate due to the relatively small number of cycles used for ensemble-averaging, highlight the temporal evolution (through one cycle) of those disturbances that are actually periodic and coherent. The jet-like effect created by the stenosis is apparent, as peak centreline velocity increases from about $1.7u_c$ at $x = -1D$ to $4.5u_c$ at the throat ($x/D = 0$) and eventually reduces to about $1.5u_c$ at $x = 8D$. These results match exactly the measurements made by Khalifa & Giddens (1981) in their study of post-stenotic disturbances for a 75 % axisymmetric stenosis.

While the centreline velocity at the throat ($x/D = 0$) maintains the precise sinusoidal nature of the inlet velocity waveform, albeit with higher peak levels because of the flow accelerating through the constriction, the waveform loses this characteristic farther downstream. The formation of the starting vortex immediately downstream of the stenosis at the beginning of the acceleration phase is manifested in the flattening of the velocity waveform at $x = 1D$, after the point of minimum flow in the cycle, $t/T \approx 0.8$. The disturbance associated with this spatially and temporally evolving start-up structure becomes more pronounced as it moves further down the vessel. At $x = 3D$ the time history plots show a well-defined disturbance associated with the passage of a fairly evolved structure during the late acceleration stage, followed by random fluctuations throughout the deceleration phase.

The subsequent breakup of the structures as they convect downstream is characterized by the high-frequency fluctuations that occur around peak flow at axial stations between $x = 4D$ and $7D$. Figure 12(*a*) indicates that the fluctuations

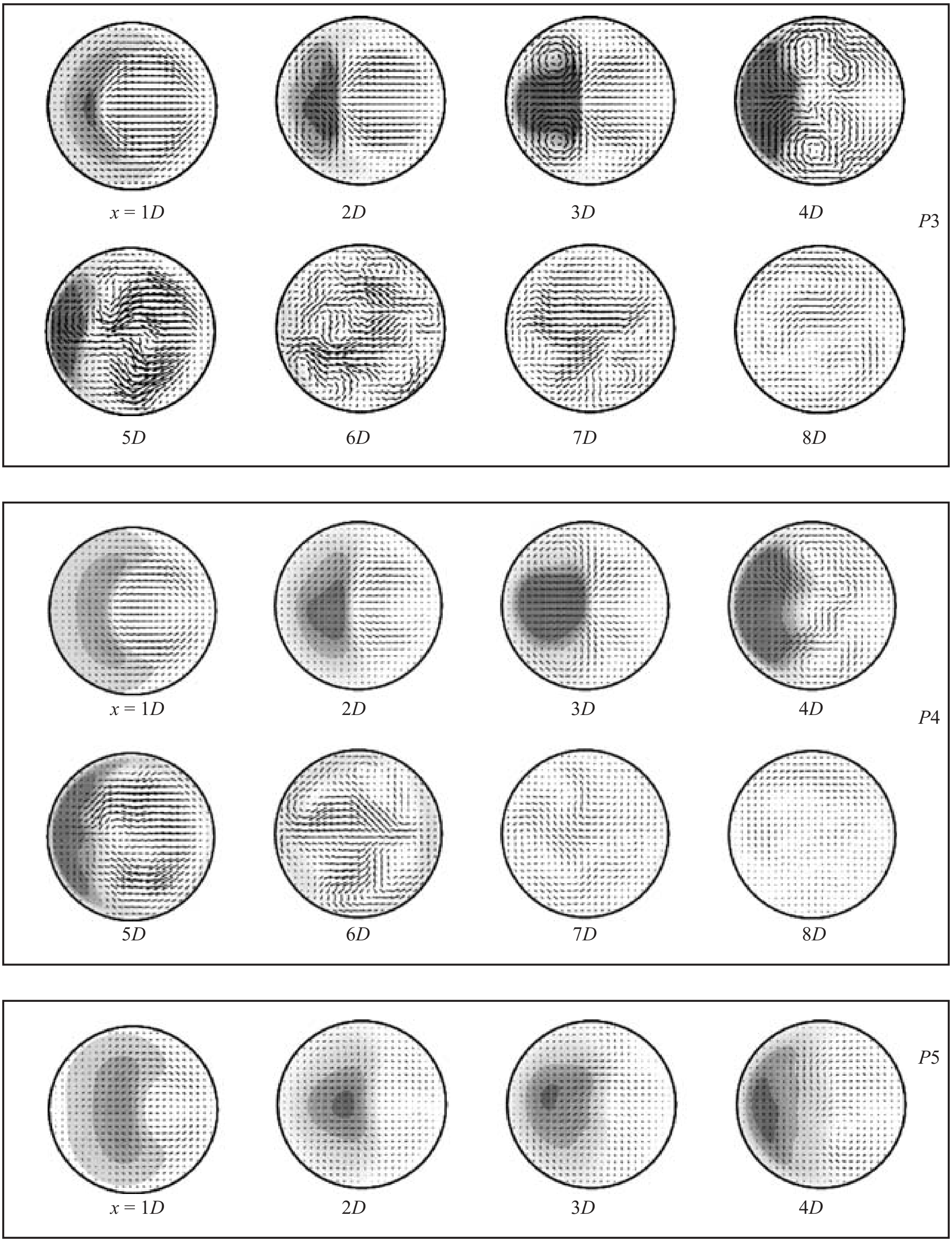

FIGURE 11. As figure 10 but during the deceleration phase and minimum flow.

grow to be particularly intense in this turbulent section of the post-stenotic vessel during the early part of deceleration and that they are repeated from cycle to cycle. The fluctuations reduce in intensity as minimum flow is approached. The ensemble-averaged velocity results in figure 12(*b*) indicate a drop in peak centreline velocity levels between $x = 4D$ and $6D$, a result of the increasing uniformity of the

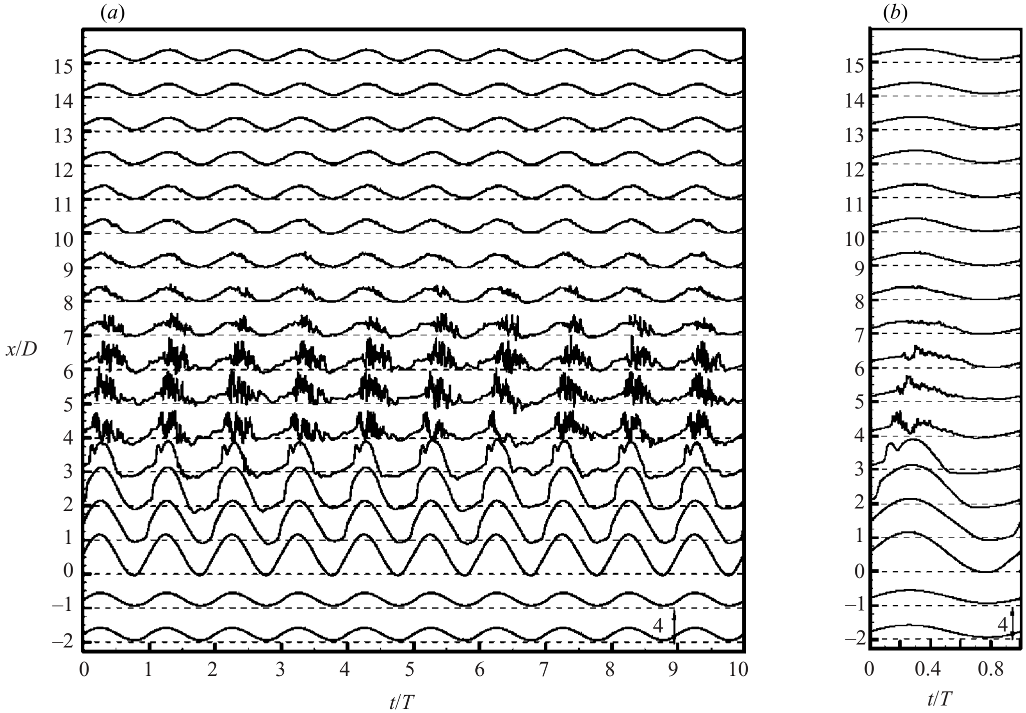

FIGURE 12. (*a*) Time history (over first 10 of the 25 cycles used for ensemble averaging) of normalized centreline axial velocity, u/u_c, as a function of axial distance for pulsatile flow through the 75 % eccentric stenosis. (*b*) Normalized ensemble-averaged centreline axial velocity, $\langle u\rangle/u_c$, as a function of axial distance.

cross-sectional velocity profile due to periodic, localized transition to turbulence. We will return to this phenomenon in § 3.2.6.

Beyond $x = 7D$, the intense fluctuations decay quite rapidly within about 4 vessel diameters, with the velocity waveforms after $x = 12D$ reverting to their laminar, upstream character. The flow field appears to be stable at all axial locations considered here during the early and mid-acceleration phases of the cycle.

3.2.4. *Turbulence statistics*

Profiles of the streamwise (u_{rms}) and cross-stream (v_{rms} and w_{rms}) r.m.s. velocities, as defined in § 2.2, are shown in figures 13, 14 and 15, respectively, providing a quantifiable measure of turbulence intensity at different times during the cycle across the entire vessel. The corresponding spatial evolution of the turbulent kinetic energy, with k defined as $\frac{1}{2}\langle u_i'' u_i''\rangle$, is shown in figure 16. Disturbance velocity and turbulent kinetic energy profiles in the upstream section of the vessel ($x < 0D$) and the far downstream region ($x > 12D$) are not included in these figures because the levels were insignificant and close to zero.

During the acceleration phase $P1$, the streamwise r.m.s. velocity profiles immediately downstream of the stenosis, most notably at $x = 2D$, exhibit peaks of almost $0.1u_c$ within the shear layer. Cross-stream disturbances, as indicated by v_{rms} and w_{rms}, in the same region are not quite as high. Farther downstream, between $x = 3D$ and $9D$, average r.m.s. levels across each section lie between 5 % and 15 % of u_c, significantly lower than the high levels the region experienced during the transitional/turbulent

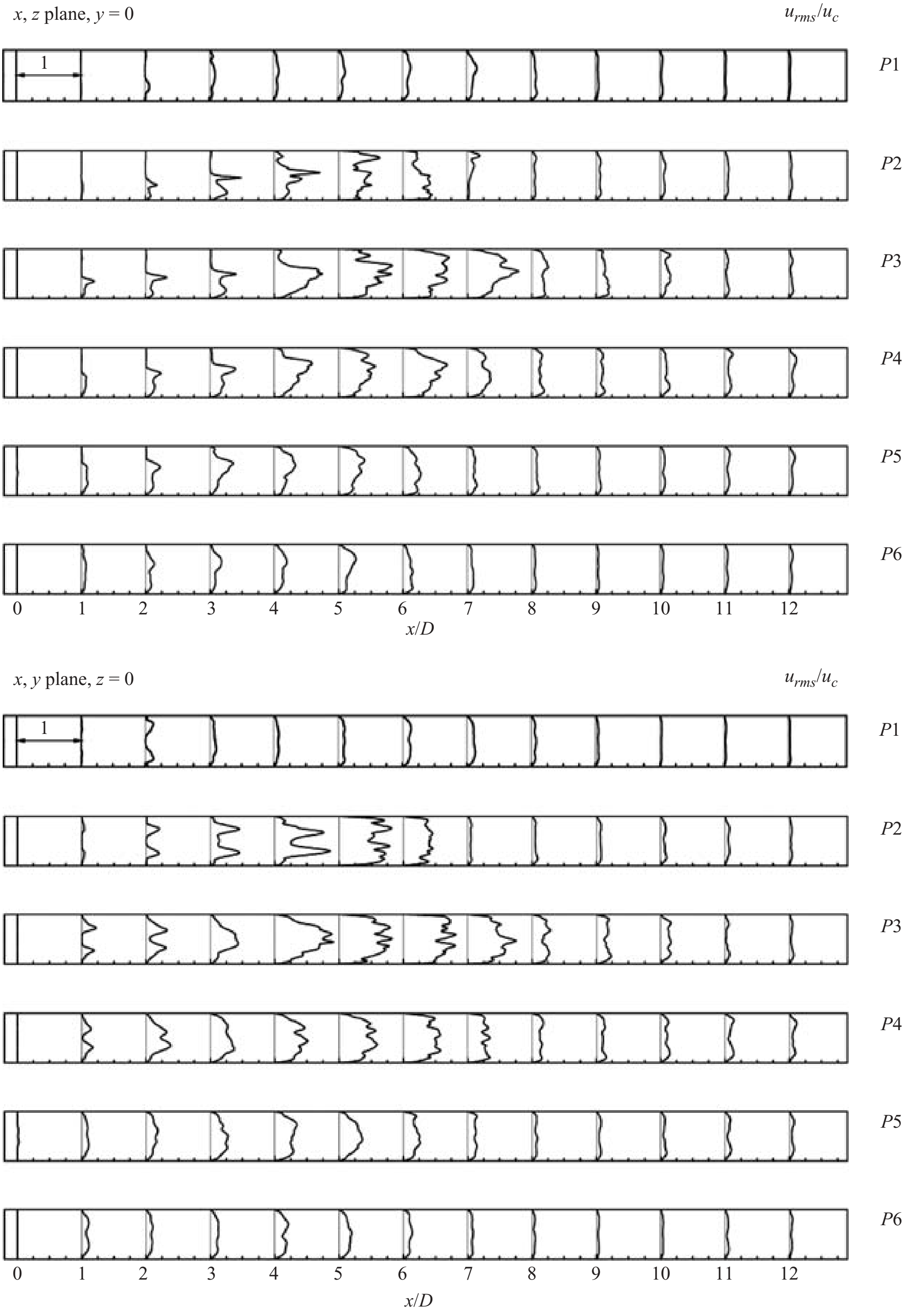

FIGURE 13. Streamwise r.m.s. velocity profiles, u_{rms}/u_c, for pulsatile flow through the 75 % eccentric stenosis.

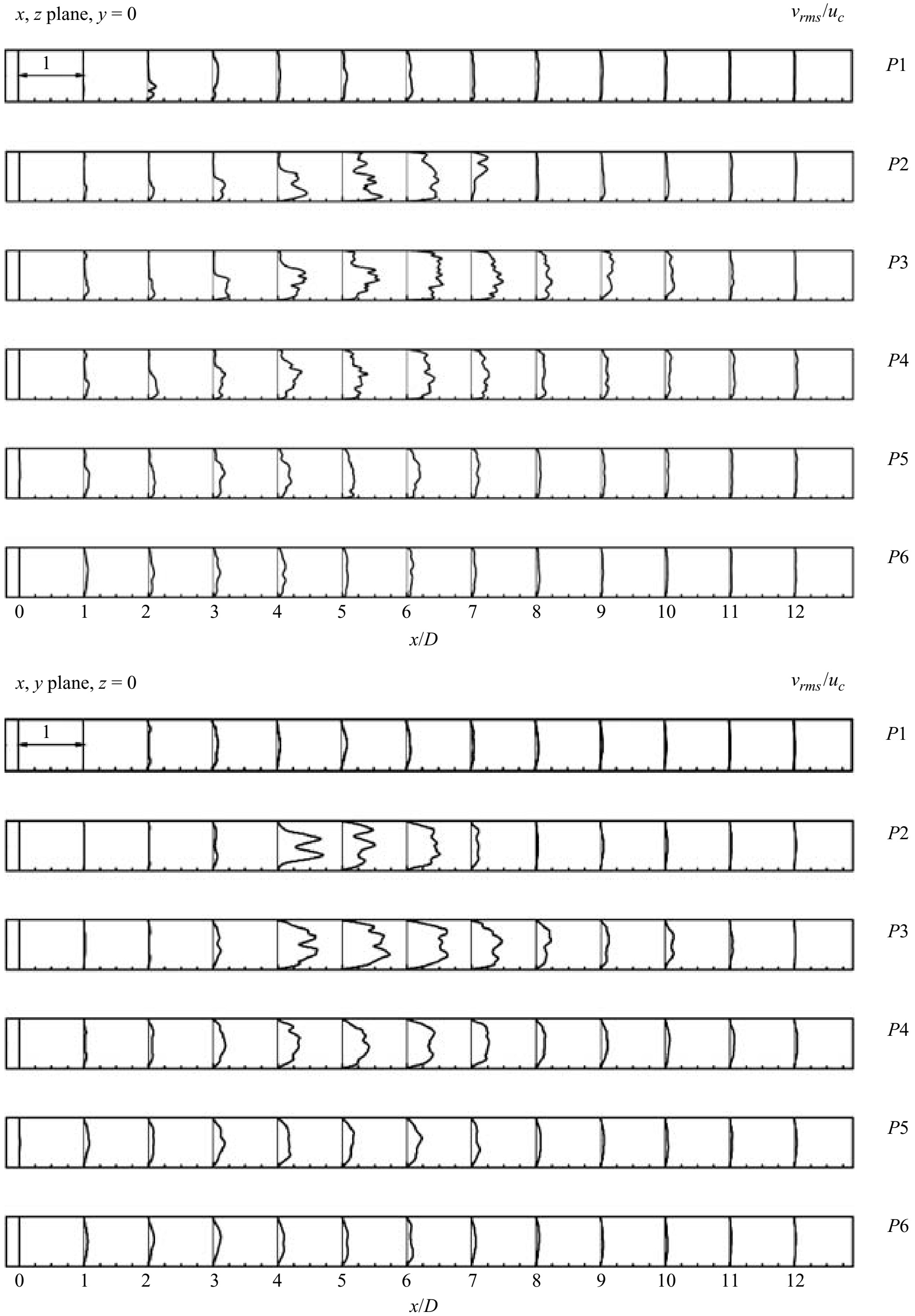

FIGURE 14. Cross-stream r.m.s. velocity profiles, v_{rms}/u_c, for pulsatile flow through the 75 % eccentric stenosis.

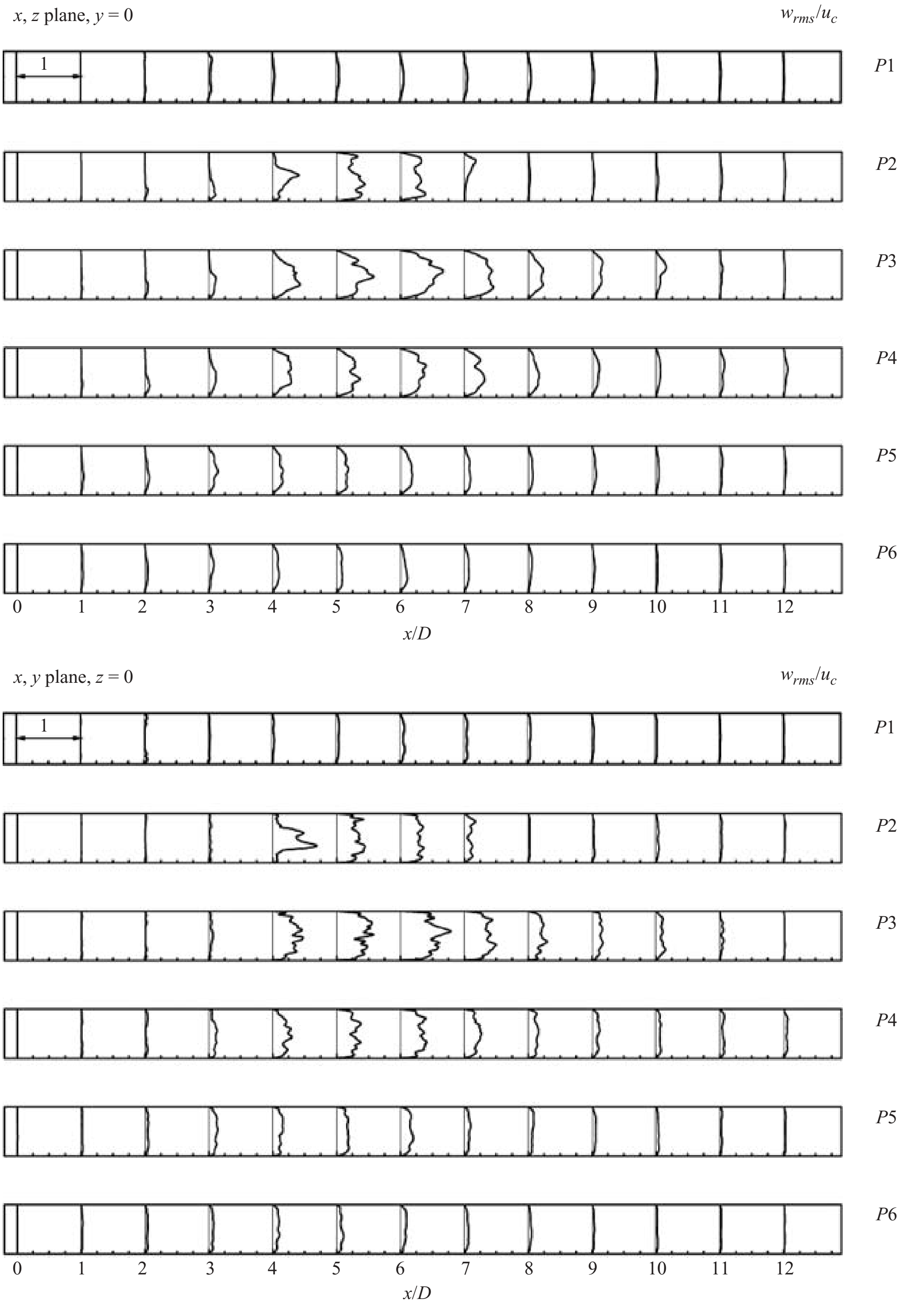

FIGURE 15. Cross-stream r.m.s. velocity profiles, w_{rms}/u_c, for pulsatile flow through the 75 % eccentric stenosis.

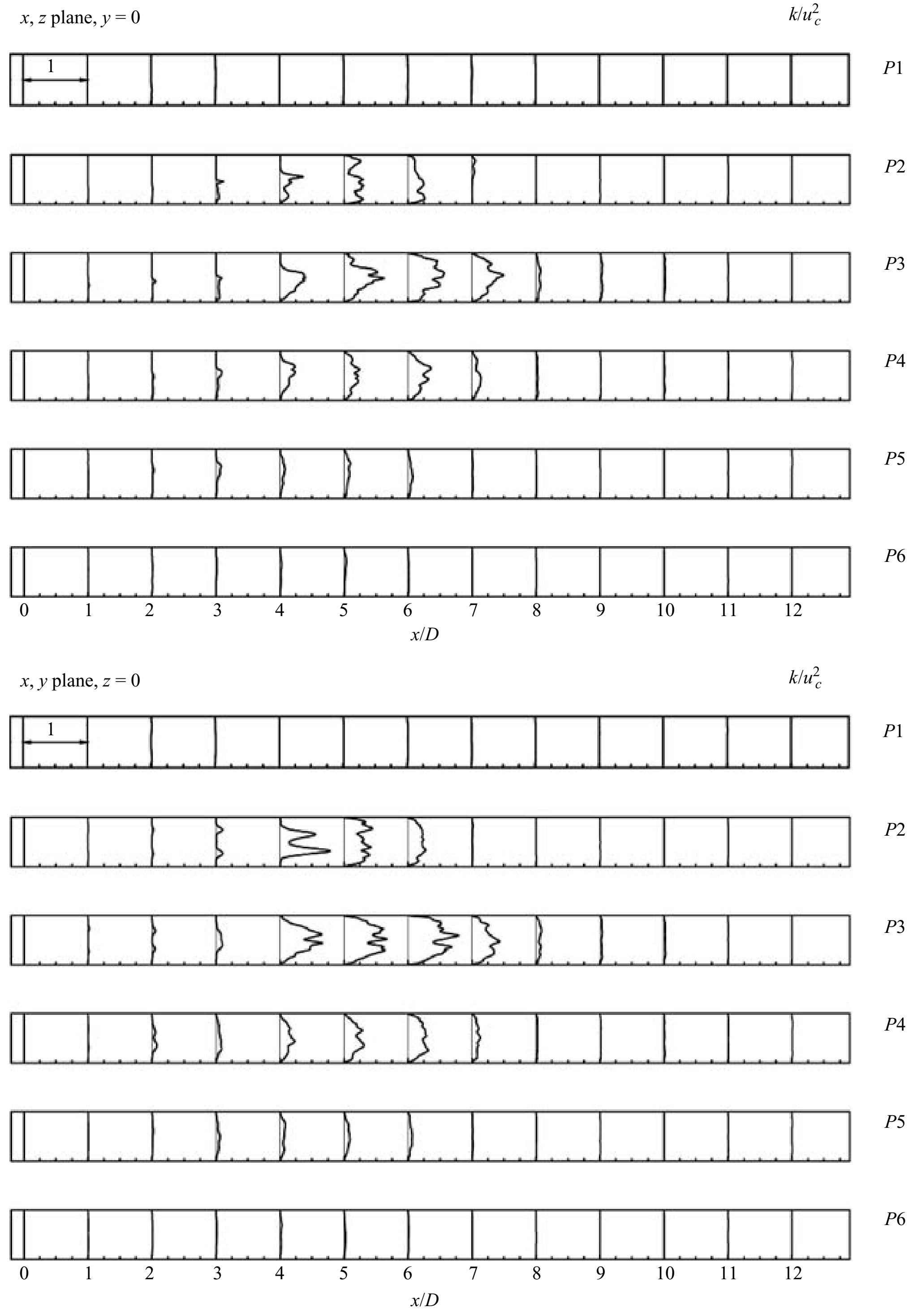

FIGURE 16. Turbulent kinetic energy (k) profiles, normalized by u_c^2, for pulsatile flow through the 75 % eccentric stenosis.

activity of the previous cycle. The turbulent energy profiles, lower than 5 % of u_c^2 across the entire post-stenotic section, confirm the progress of relaminarization throughout the acceleration phase.

At the end of acceleration, culminating in peak flow conditions at the inlet ($P2$), there is a sharp amplification of the disturbance and turbulent energy levels, especially within the shear layer. As figure 13 illustrates, peak values of u_{rms} in the $y=0$ plane increase with axial distance, from about $0.25u_c$ at $x=2D$ to more than $0.4u_c$ and $0.75u_c$ at $x=3D$ and $4D$, respectively, while turbulent energy peaks at about $0.75u_c^2$ at the latter station. The subsequent jet breakdown after it encounters the wall spreads over the entire cross-section of the vessel, as a result of which both streamwise and cross-stream *r.m.s* velocity profiles at $x=5D$ and $6D$ exhibit more uniformity than their immediate upstream counterparts, with mean levels now larger than $0.25u_c$. Turbulent energy profiles at the same locations show turbulent energy peaking at $x=5D$, the axial station at which the shear layer completely breaks up at this stage. While maximum turbulence intensities occur in the shear layer immediately downstream of the stenosis after peak flow, it is clear from comparing the phase-averaged axial velocity profiles in figure 8 with u_{rms} profiles in figure 13 that the disturbance levels within the recirculation regions also start to rise during this stage. The most intense reverse flow regions experience peak u_{rms} levels of $0.25u_c$ or higher. Figures 14 and 15 indicate that cross-stream r.m.s. velocity levels, which are lower than $0.1u_c$ within the shear layer, are higher in these zones, with v_{rms} as high as $0.25u_c$ and $0.5u_c$ at $x=3D$ and $4D$, respectively. The turbulent energy profiles in the $y=0$ plane also indicate a fairly significant level of turbulence within the recirculation region at this time, with a peak of almost $0.2u_c^2$ at $x=4D$ close to the wall.

During the early deceleration stage $P3$ there is a significant increase in turbulent energy levels between $x=4D$ and $7D$, indicating that the transition to turbulence process accompanying jet breakdown now extends over a larger section of the post-stenotic vessel. All three components of the r.m.s. velocity in this turbulent region are comparable, with average levels of about $0.25u_c$ at $x=4D$ and $0.5u_c$ at $x=6D$ before dropping back to less than $0.25u_c$ after $x=8D$. The maximum turbulence intensity is experienced during this phase of the pulsatile cycle in the region between $x=5D$ and $6D$, with peak values of u_{rms} more than 100 % of u_c and turbulent energy peaks larger than $0.75u_c^2$. As the flow continues to decelerate, turbulence intensity starts to reduce, with average r.m.s. and turbulent energy levels in the turbulent section during phase $P4$ dropping to less than half their pre-mid-deceleration levels. Throughout the deceleration phase, mean r.m.s. levels within the recirculation regions between $x=2D$ and $4D$ lie in the range 0.1–$0.2u_c$, even though turbulent energy within these zones is lower than $0.1u_c^2$, not quite as large as that observed during peak flow conditions.

By the point of minimum inlet flow, $P5$, turbulent energy levels decrease sharply to less than $0.1u_c^2$ at all stations. The streamwise r.m.s. velocity drops to about $0.25u_c$ between $x=4D$ and $6D$, while average cross-stream levels at these locations also drop to less than $0.15u_c$, even as the relaminarization process starts with the reversal of the pressure gradient at this time and continues into the acceleration phase. Mean r.m.s. levels during the early acceleration $P6$ are less than 10 % of u_c across the entire downstream region and remain so throughout the rest of this phase, though they indicate the presence of small disturbances even in the absence of turbulence.

Disturbance levels are clearly negligible throughout the acceleration phase in the region beyond $x=9D$. Only during deceleration do r.m.s. levels between $x=9D$ and $12D$ increase, with mean values of about $0.1u_c$ at the former station and even less

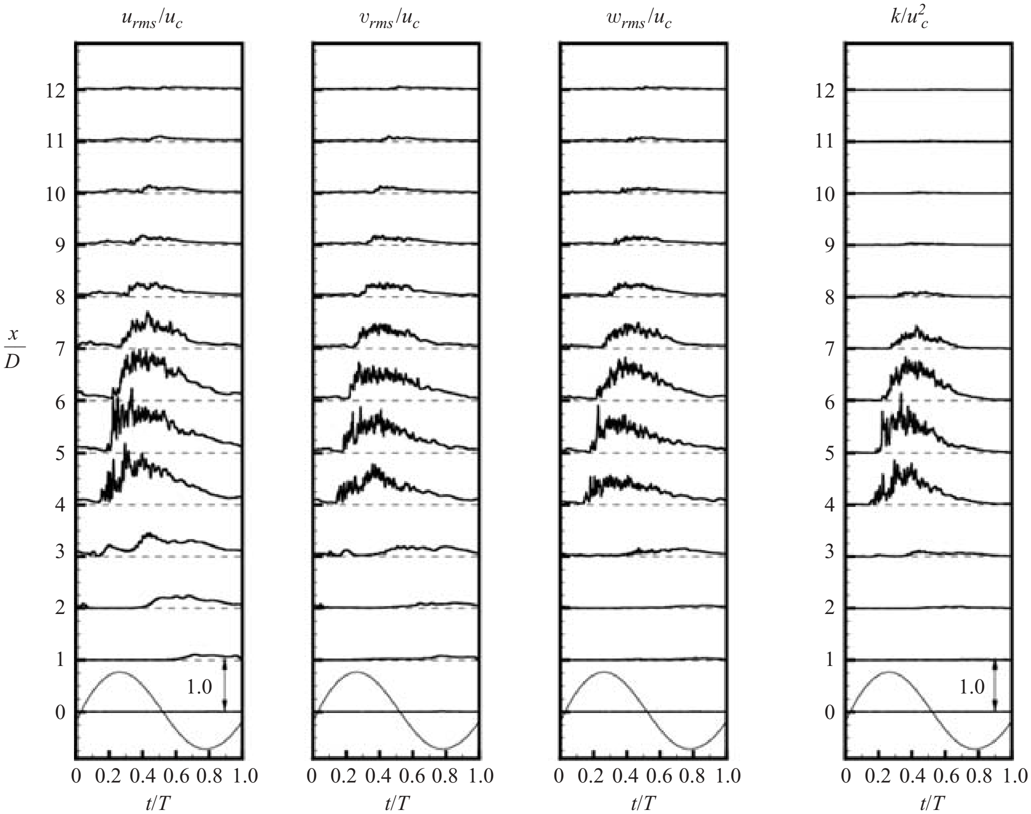

FIGURE 17. Time evolution of r.m.s. velocities and turbulent kinetic energy over the pulsatile cycle at axial stations along the vessel centreline for pulsatile flow through the 75 % eccentric stenosis. The inlet flow waveform has been superimposed on the profile at $x/D = 0$ in order to analyse statistics during different parts of the cycle.

at the latter. Turbulent energy levels in this far-downstream section are close to zero throughout the cycle, indicating that the flow reverts quite rapidly to its upstream laminar state downstream of the turbulent section.

Figure 17 shows the variation of all three components of r.m.s. velocity and turbulent kinetic energy along the centreline of the vessel during a pulsatile cycle, providing insight into the temporal evolution and periodicity of these turbulence parameters. In the immediate downstream locations, at $x = 1D$ and $2D$, streamwise disturbances rise to about $0.2u_c$ during the late deceleration stage, around minimum flow. This corresponds to the phase during which these locations experience reverse flow, as the phase-averaged centreline axial velocity results in figure 12 show. At $x = 3D$, the passage of a starting structure during the late acceleration phase is associated with u_{rms} levels of about $0.25u_c$, subsequently increasing to almost $0.5u_c$ during peak flow, when breakdown starts to occur. Past mid-deceleration, when the reverse flow regions extend to the centreline at this station, cross-stream disturbances also rise to almost $0.25u_c$, comparable to the streamwise disturbances during this time, along with a corresponding increase in turbulent energy levels to about $0.1u_c^2$.

Farther downstream, for $x > 3D$, the start of the turbulent jet breakdown process at peak flow is accompanied by large streamwise r.m.s. velocities, which at this time are almost a factor of 2 larger than their cross-stream counterparts. Turbulence intensity along the centreline clearly reaches a maximum during the early deceleration stage, with u_{rms} and energy levels attaining peaks that are as high as 100 % of u_c and $0.75u_c^2$, respectively, between $x = 4D$ and $6D$. Cross-stream r.m.s. levels in the turbulent zone are of comparable magnitude to the streamwise levels during the remainder of deceleration, the latter dropping to about $0.5u_c$ by mid-deceleration and $0.25u_c$ by minimum flow. Turbulent energy levels in this region also decrease sharply during this stage and are close to zero throughout most of the acceleration phase. Centerline disturbance and energy levels are lower at $x = 7D$ and $8D$, with all statistics rising significantly only during deceleration, when transition to turbulence takes place immediately upstream of these stations. Beyond these locations, in the far downstream region, disturbance and energy levels are mostly insignificant throughout the cycle, as seen earlier while studying the profiles.

3.2.5. *Energy spectra*

Results presented for the steady flow case showed that energy spectra can aid in providing additional information about the nature of disturbances in the post-stenotic region. For the current pulsatile flow results, the normalized spectrum, E^*, and Strouhal number, N_s, have been defined by using the conventions followed in similar studies (Cassanova & Giddens 1978; Khalifa & Giddens 1981; Mittal *et al.* 2003) as

$$E^* = \frac{E(f)u_p}{2\pi d}, \qquad N_s = \frac{2\pi f d}{u_p}, \tag{3.1}$$

respectively. $E(f)$ is the frequency spectrum of the normalized streamwise velocity fluctuations $(u''/u_{rms})^2$, f is the frequency of the fluctuation, d $(= 0.5D)$ is the minimum stenosis diameter and u_p is the peak cross-sectional average velocity at the stenosis throat, calculated as $\approx 4.3u_c$ using Womersley's analysis (Womersley 1955). Cassanova & Giddens (1978) postulated that d and u_p are appropriate scaling parameters for the spectra because it is the peak stenotic jet velocity that initiates the transition to turbulence in the downstream section.

The frequency spectra $E(f)$ of the velocity data in figure 12(*a*) were computed by using Welch's overlapping averaged modified periodogram method (Welch 1967). The data were divided into 25 segments with 50 % overlap, each section windowed with a cosine taper window (Hann window) to reduce leakage, and 25 modified periodograms were computed and averaged. The data sampling rate was 2 kHz (every two time-steps), corresponding to a Nyquist frequency of 1 kHz.

Figure 18 shows the computed normalized centreline disturbance energy spectra at various axial stations downstream of the stenosis throat. As in the steady flow spectra in Part 1, the lines corresponding to $N_s^{-5/3}$ and N_s^{-7} have been included in the figure, the former characterizing the inertial subrange, where energy cascades from the large eddies to smaller ones with minimal energy dissipation, and the latter the viscous dissipation range (Tennekes & Lumley 1972; Hinze 1975; Wilcox 1993; Mittal *et al.* 2003). Studies of post-stenotic flow by Kim & Corcoran (1974) and Lu, Gross & Hwang (1980) have found evidence of a $N_s^{-10/3}$ range in the velocity spectra, also indicated in the figure, with the latter group observing that *in vivo* velocity spectra fell from a −5/3 to −10/3 slope at a frequency associated with arterial murmurs.

The spectrum immediately downstream of the stenosis is quite different from those observed under steady inlet flow conditions, where there were well-defined peaks concentrated within a narrow frequency range due to passage of vortices. There is

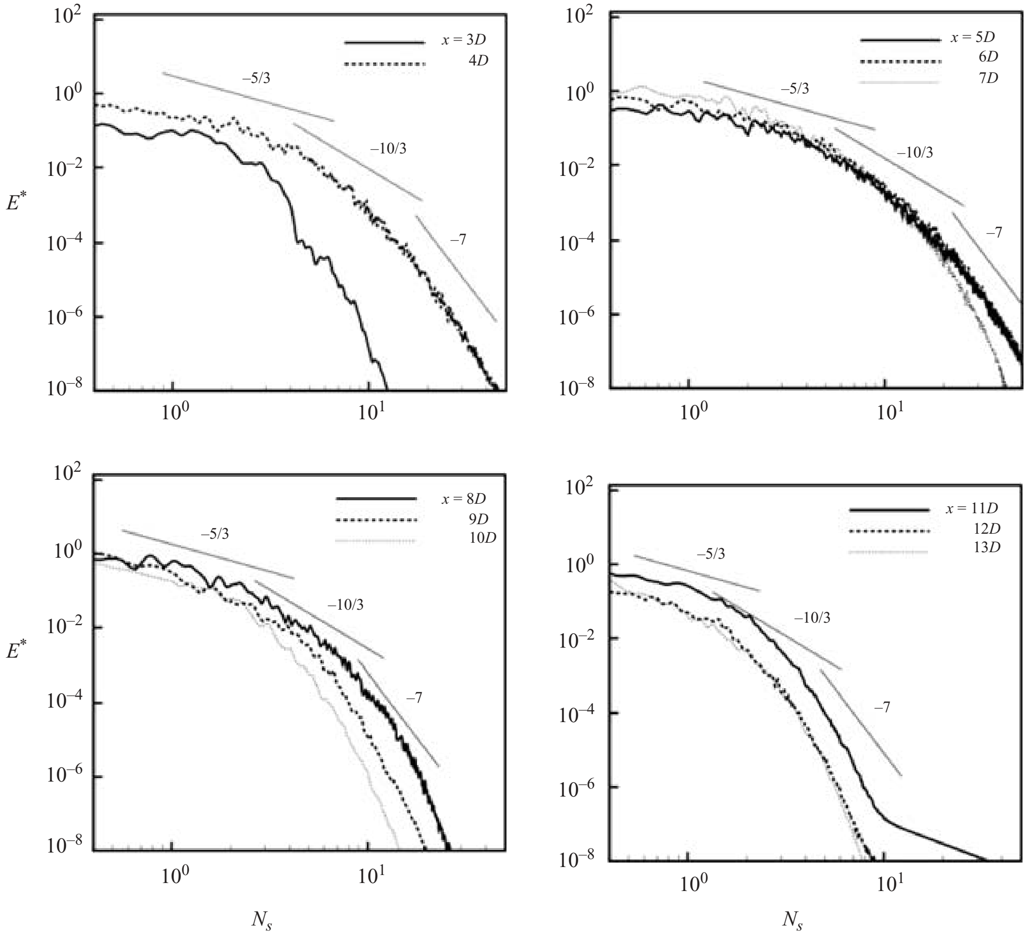

FIGURE 18. Energy spectra of centreline streamwise velocity fluctuations, u'', normalized by centreline u_{rms} at the same locations, for pulsatile flow through the 75 % eccentric stenosis.

clearly no such phenomenon at $x = 2D$ for the pulsatile case. Further downstream, at $x = 3D$, the spectrum starts to take on a more broadband nature as turbulent breakdown starts. However the spectrum rolls off rapidly after $N_s \approx 3.0$ from a $-5/3$ slope to a -7 slope, indicating that transition to turbulence is not complete.

The flow clearly transitions to broadband turbulence at $x = 4D$, with the spectra at this location indicating a relatively larger range of frequencies constituting the inertial subrange. The spectrum rolls from this range to a $-10/3$ slope rather gradually, after $N_s \approx 4.5$, eventually attaining a slope of -7 at frequencies higher than 10.0. The energy distributed at higher frequencies rises even farther after $x = 4D$, as the increasingly broadband spectra at $x = 5D$ and $6D$ highlight. The spectra at these stations roll off to a $-10/3$ slope at frequencies of approximately 5.5 and 7.0, respectively, the large range of frequencies comprising the inertial subrange indicative of fairly well-developed turbulent flow in this region. Turbulence intensity drops rapidly farther downstream, with the spectra at $x = 7D$ and $8D$ rolling from the $-5/3$ range to a $-10/3$ slope at $N_s \approx 4.0$ and 3.0, respectively. With viscous effects dominating the region beyond $x = 8D$ and relaminarization taking place, the spectra in the far downstream region roll off into the viscous dissipation range at frequencies as low as $N_s \approx 2.5$. Clearly, the $-10/3$ range is largest within the turbulent part of the post-stenotic flow field, between $x = 4D$ and $8D$, and is almost absent in the region $x > 9D$, consistent with the speculation that arterial murmurs are closely associated with turbulent flow within these arteries.

3.2.6. *Turbulence structure*

In this section we consider some of the interesting features of the turbulence structures alluded to in the previous sections while discussing the spatial and temporal evolution of averaged flow characteristics and turbulent statistics. Figures 19 and 20 show instantaneous coherent structures, as identified by isosurfaces of a negative contour of the λ_2 criterion of Jeong & Hussain (1995). Corresponding instantaneous contours of the streamwise velocity fluctuations u''/u_c are depicted in figure 21.

During the late acceleration phase $P1$, the λ_2 structures in figure 19 clearly show the vortex ring, which had formed at the front of the stenotic jet earlier during acceleration, starting to deform and stretch in the streamwise direction between $x = 2D$ and $3D$. The corresponding streamwise velocity fluctuations are less than 15 % of u_c across the entire downstream section of the vessel, indicating fairly quiescent flow during this time. As the flow becomes increasingly unstable throughout the end of the acceleration phase, the starting vortex breaks into elongated smooth streamwise structures that extend axially over a length of more than one vessel diameter. These vortices eventually break down into small-scale structures at $x = 4D$ when the flow rate reaches its peak at $P2$. By the advent of peak flow, relatively strong fluctuations are present in the shear layer between $x = 2D$ and $4D$. The unstable shear layer can be seen to rollup before bursting into a localized turbulent spot that occupies the entire cross-section of the vessel between $x = 4D$ and $6D$. This spot-like transition of elongated streamwise structures has also been observed by Scotti & Piomelli (2001) in their DNS studies of pulsating turbulent channel flow at low frequencies. Streamwise vortices have been shown to play an important role in the transition mechanism of stable shear and pipe flows by several investigators (Waleffe 1997; Eliahou, Tumin & Wygnanski 1998; Shan *et al.* 1999; Han, Tumin & Wygnanski 2000). These longitudinal rolls redistribute the streamwise momentum across the cross-stream directions, causing non-uniformity and rendering the flow unstable even with respect to small three-dimensional disturbances.

Figures 20 and 21 indicate that turbulent breakdown of the structures continues into the early stages of deceleration with the turbulent spot occupying the entire region between $x = 4D$ and $7D$ during phase $P3$. Fluctuation levels within the shear layer can be seen to be rising to a maximum during deceleration, even as the intensity of the breakdown starts to drop as the flow loses its momentum and moves past the mid-deceleration stage toward minimum flow. The turbulent spot clearly loses its strength by phase $P4$, as deceleration progresses, and almost completely loses its identity by the point of minimum flow at $P5$. The relaminarization process starts during late deceleration itself; as a result, the subsequent acceleration phase starts with relatively low residual fluctuation levels. Figure 19 shows the formation of a new vortex ring immediately downstream of the stenosis throat during phase $P6$ as the flow once again starts to pick up momentum, while the remainder of the downstream section continues to undergo relaminarization.

The variation of instantaneous streamwise velocity along the vessel centreline for the eccentric model is shown in figure 22. Corresponding results for the laminar, axisymmetric case are also included in the figure to highlight the footprints left by

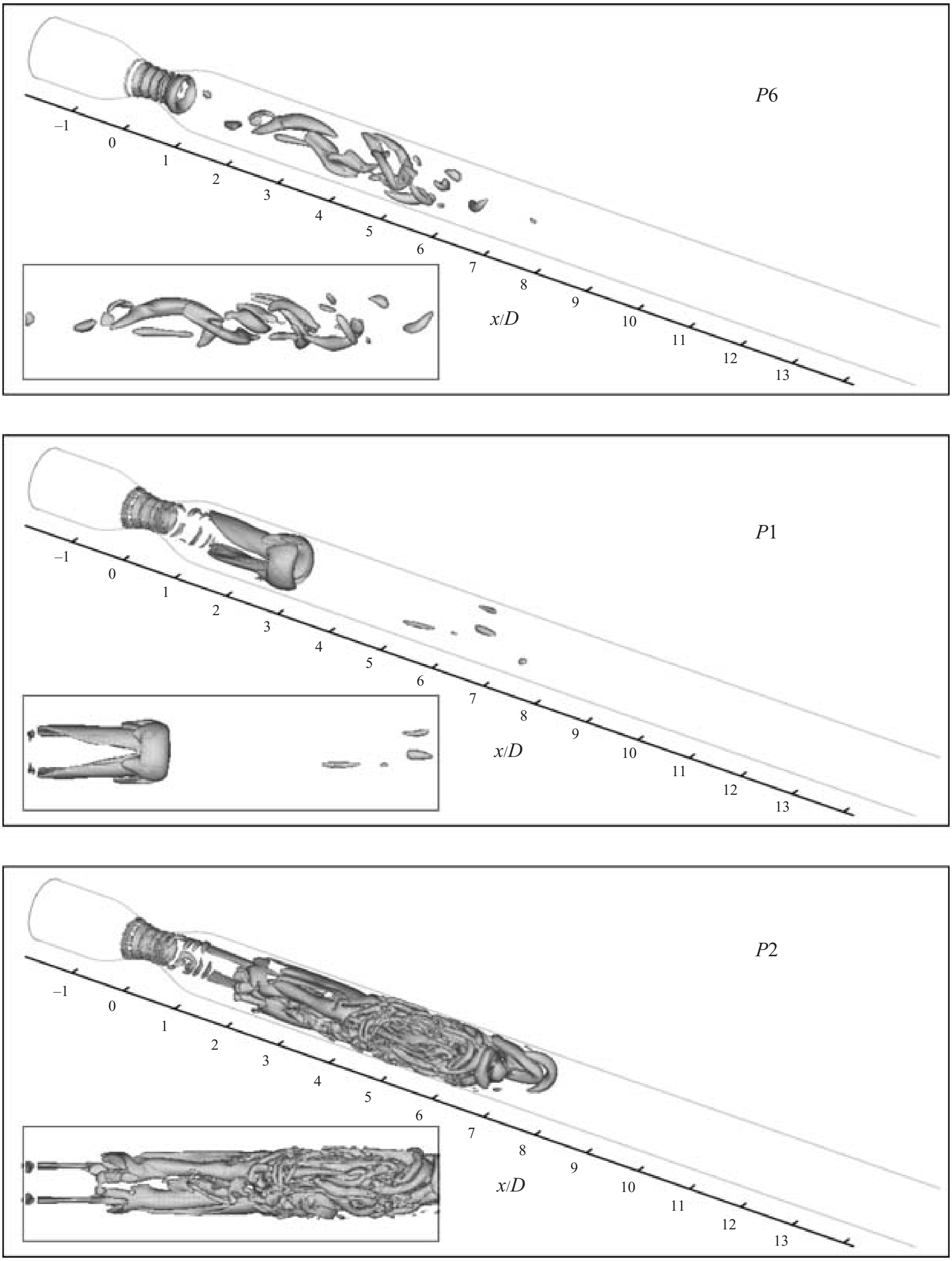

FIGURE 19. Sequence of instantaneous coherent structures (vortices) during acceleration and peak flow stages for pulsatile flow through the 75 % eccentric stenosis. The structures are identified by using the isosurface corresponding to the negative contour −1.25 of the λ_2 criterion of Jeong & Hussain (1995), normalized by u_c/D. The inset in each plot shows a close-up view of the structures in the region $1D \leqslant x \leqslant 6D$.

the turbulent structures in the eccentric case. The flow field is clearly laminar during the late acceleration phase $P1$, with centreline velocities for the eccentric model closely matching its laminar counterpart. The velocity reaches a peak at the throat before

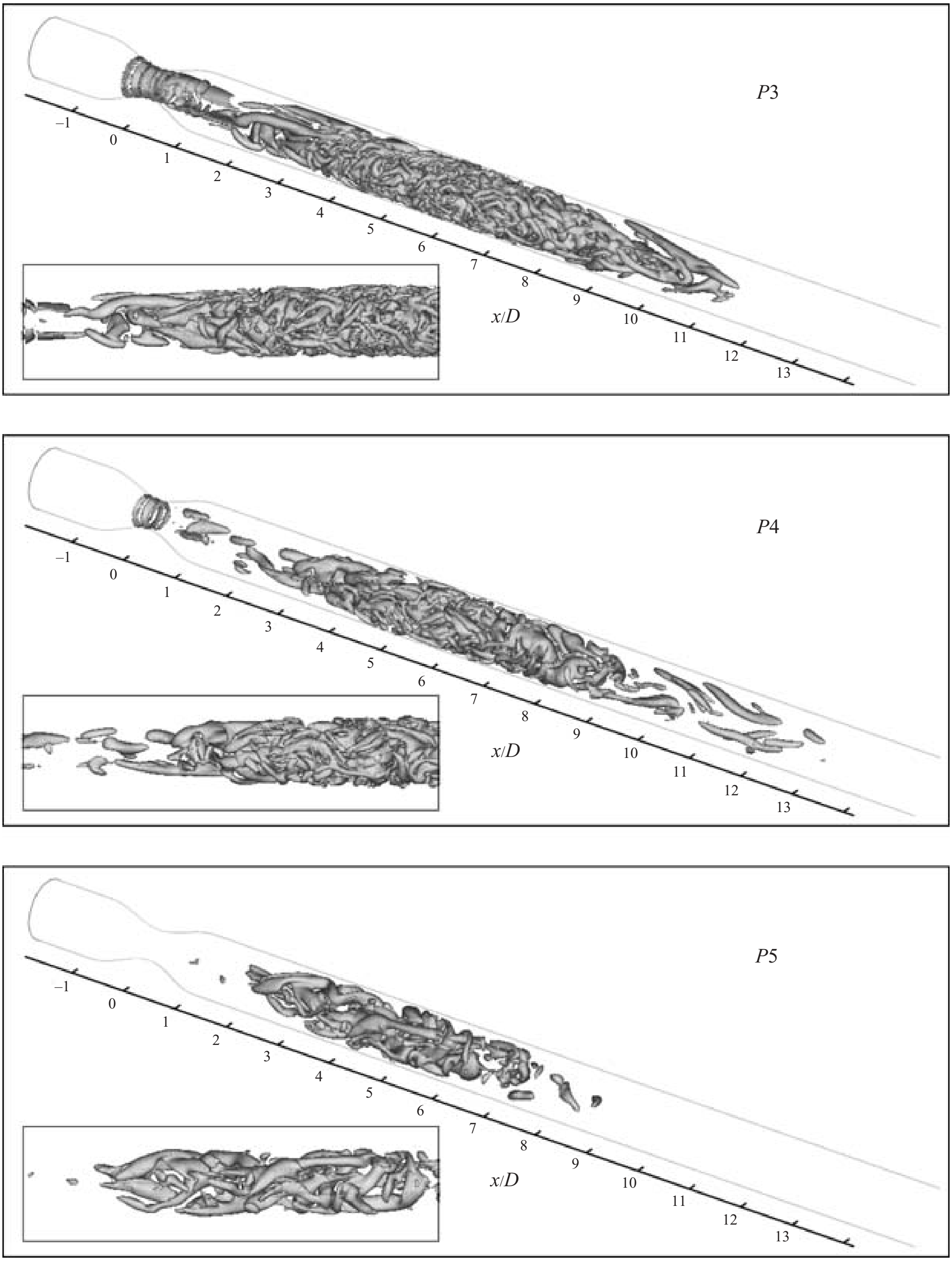

FIGURE 20. Sequence of instantaneous coherent structures during deceleration and minimum flow of the cycle for pulsatile flow through the 75 % eccentric stenosis. The structures are identified by using the same λ_2 criterion as in figure 19 and the insets show a close-up view in the region $1D \leqslant x \leqslant 6D$.

falling back to normal levels in the downstream section, following flow reattachment at the walls (at $x \approx 3D$). Residual disturbances from the previous cycle are clearly present in the region beyond $x = 7D$, where centreline velocities are lower than

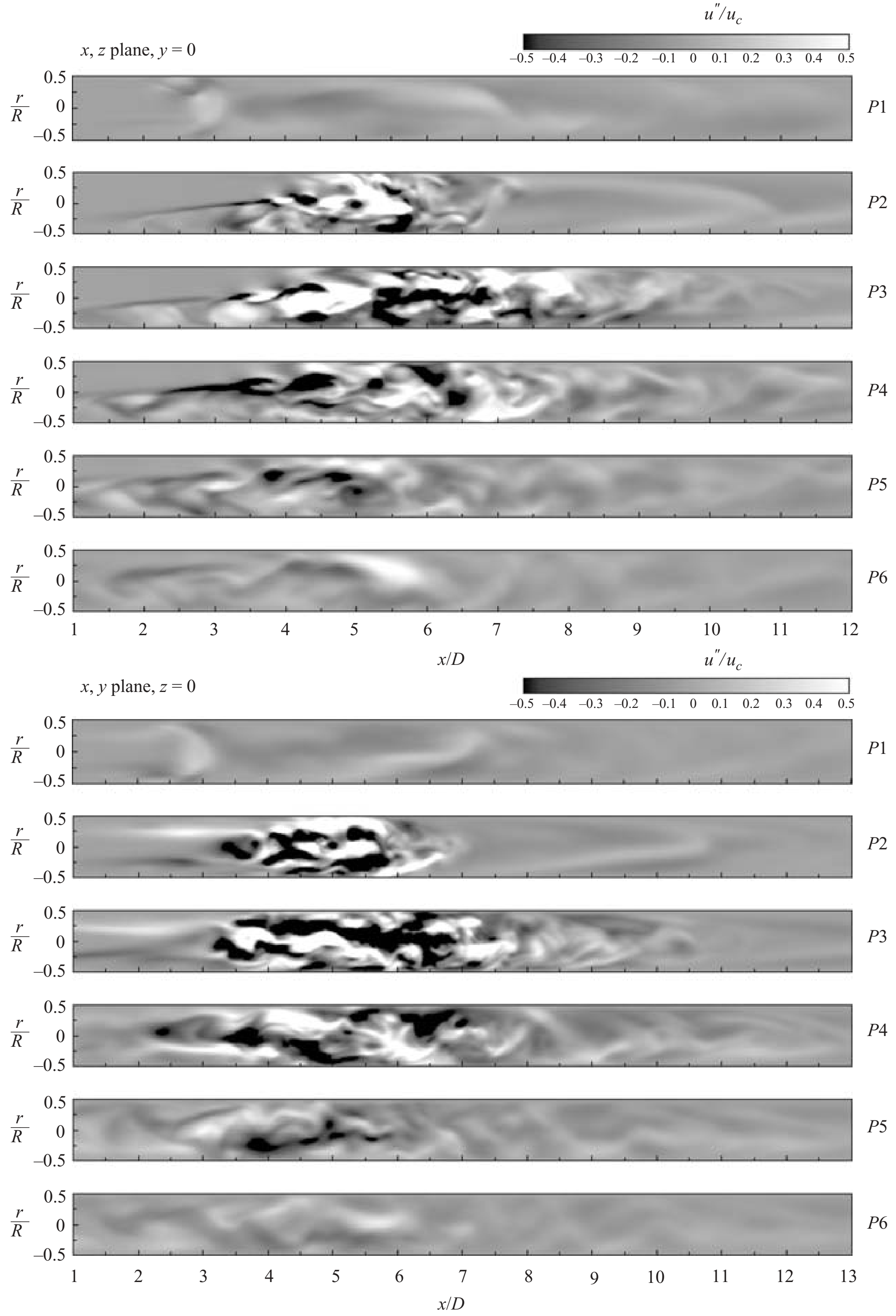

FIGURE 21. Sequence of contours of the instantaneous streamwise velocity fluctuations u''/u_c, for pulsatile flow through the 75 % eccentric stenosis.

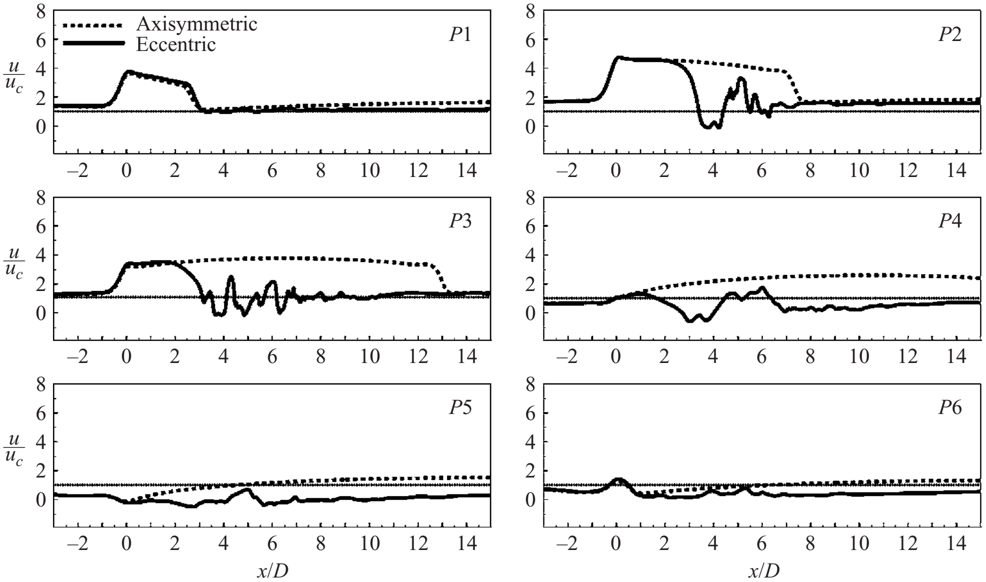

FIGURE 22. Variation of instantaneous streamwise velocity u/u_c along the centreline of the vessel, for pulsatile flow through the 75 % axisymmetric and eccentric stenosis.

laminar levels, indicating that the flow field has not quite achieved complete relaminarization.

Breakdown into turbulence after $x = 3D$ at peak flow ($P2$) is accompanied by a sharp drop in centreline velocity, as a result of the change in the velocity profile, from laminar upstream of the turbulent spot to a fuller turbulent flow profile inside it. The velocity signatures are in good agreement with the results of Stettler & Hussain (1986), who investigated transition in pulsatile pipe flows. The traces show the turbulent spot, or patch as they termed it, having a sharp leading front (closer to the stenosis). The apparent 'jetting' action of the laminar fluid into the turbulent patch produces the roll-up seen in the streamwise fluctuations of figure 21, followed by high-intensity fluctuations as turbulent breakdown occurs between $x = 4D$ and $6D$. After this breakdown, the absence of any mechanism to continue producing turbulence results in the fluctuations decaying and the flow relaminarizing, and so the trailing edge of the spot (farther from the stenosis) is not quite as well defined. This is in contrast to the signatures left by puffs and slugs in the transition regime of steady pipe flows (Wygnanski & Champagne 1973; Wygnanski, Sokolov & Friedman 1975). The former is characterized by a gradual drop in the centreline velocity as laminar flow transitions into high-frequency turbulent fluctuations within the interior of the puff. The fluctuation level drops at the trailing edge, and the velocity increases rapidly. On the other hand, a slug is associated with abrupt transition between laminar and turbulent flow at the beginning and end of the turbulent region, in relation to its duration.

During the deceleration phase ($P3$ through to $P4$), the centreline velocity deficit starts to become less distinct when compared with the traces at peak flow. The reason is that the flow rate drops during this time, and the profiles become flatter and less jet-like as a result; in other words, the difference between the centreline and mean velocity at a particular axial station starts to reduce. Hence, the jetting action is considerably weakened. Throughout the deceleration phase, the λ_2 structures in figure 20 show the presence of hairpin-like vortices near the trailing-edge region of the turbulent spot.

It appears that these streamwise vortex pairs serve to exchange fluid between the turbulent and laminar regions, contributing to the relaminarization process as the flow rate continues to drop. The intensity of turbulent fluctuations decays rapidly after the mid-deceleration phase, and under minimum inlet flow conditions at phase $P5$ the fluctuations are almost completely absent. However, the flow field has not completely relaminarized even by the early acceleration phase $P6$, with centreline velocities lower than normal.

Velocity results in figure 22 indicate that there is insufficient time for the entire post-stenotic section to regain its normal laminar state. Only in the far downstream region, $x > 8D$ under peak flow conditions and $x > 12D$ during early deceleration, do centreline velocities achieve their laminar values, indicating that the velocity profiles at these locations have indeed reverted to their natural undisturbed character. However, these disappear later in the cycle as residual disturbances from the turbulent post-stenotic region convect into the far downstream flow field.

3.3. *Wall shear stress*

The flow features discussed in the previous sections are directly manifested in the wall shear stress (WSS) patterns across the entire vessel. Low and oscillatory WSS in particular has been implicated in arterial disease progression (Ku 1997). Figures 23 and 24 show the variation of axial WSS for both the axisymmetric and eccentric model at different phases during the cycle, scaled by time-averaged (over the entire cycle) upstream values to reveal the variations in shear in relation to normal, healthy arterial levels. WSS in the case of the eccentric stenosis has been ensemble-averaged. The circumferential locations at which the shear stresses were obtained are also indicated in the figures.

Figure 23 shows that WSS levels for the axisymmetric and eccentric models are virtually identical until about $0.5D$ downstream of the throat. During the late acceleration phase and even into early deceleration, the large velocities at the throat give rise to extremely high WSS levels within the stenosis itself. From a level of about 55 times time-averaged upstream values during phase $P1$, WSS increases by a factor of almost 75 under peak inlet flow conditions ($P2$) before dropping back to about 45 during the early deceleration phase $P3$. The increase during peak inlet flow corresponds to almost a factor of 30 increase from its immediate upstream levels (at $x = -1.5D$), matching very well with the experimental measurements of Ahmed & Giddens (1984).

With flow separation starting to occur in the diverging section, shear levels drop rapidly and stresses become negative. As one would expect, the results for the eccentric model clearly indicate that WSS is highly asymmetric across the circumference of the post-stenotic wall, unlike its axisymmetric counterpart. For both models, flow reattachment results in a dip, followed by a subsequent jump, in the WSS profile during phase $P1$. In the case of the axisymmetric model, this travels further downstream with the reattachment location as the cycle progresses. While circumferential variations are not significant during acceleration, localized transition to turbulence under peak inlet flow conditions results in the WSS profiles for the eccentric model departing significantly from the laminar axisymmetric profiles. Ensemble-averaged WSS for the eccentric case show large axial and circumferential gradients as the stenotic jet is deflected towards the wall, resulting in high WSS on this side and negative values on the opposing side where flow separation occurs. Further downstream, when the jet starts to break down in the region between $x = 3D$ and $5D$, shear levels are mostly low and negative. Early flow reattachment as a consequence of transition results in

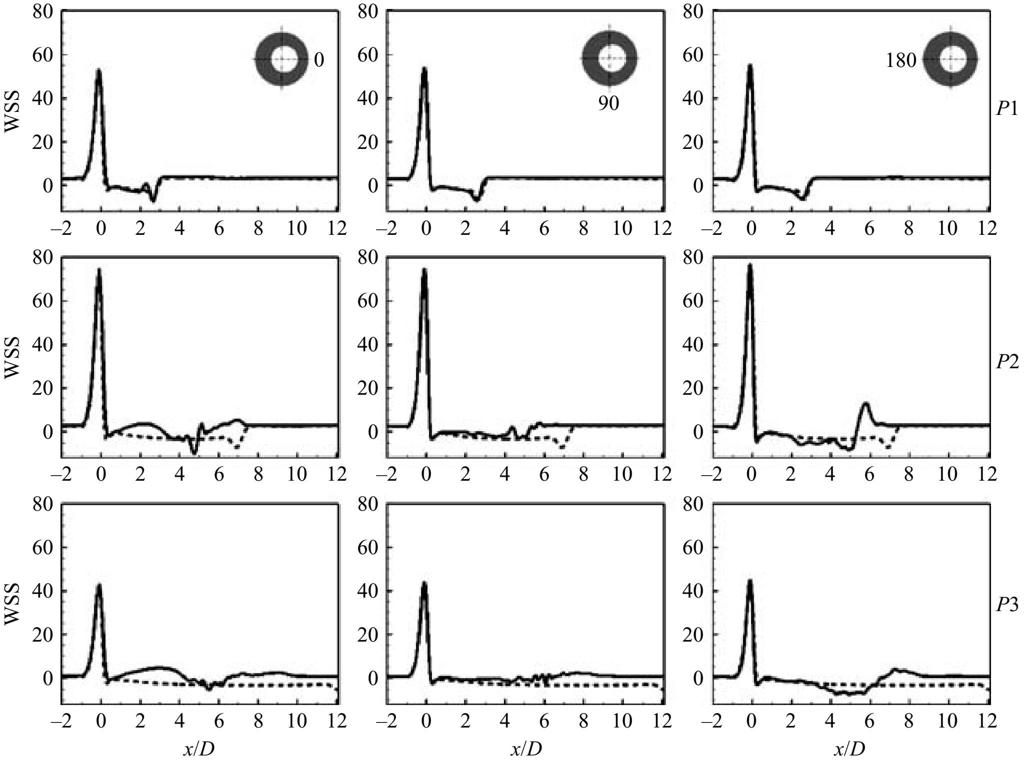

FIGURE 23. Axial wall shear stress during phases $P1$, $P2$ and $P3$, normalized by time-averaged (over the entire cycle) values upstream of the stenosis. The dashed line denotes WSS levels for the axisymmetric model while the solid line corresponds to phase-averaged WSS for the eccentric model. The circumferential locations at which WSS was obtained are indicated.

WSS attaining upstream levels earlier than in the laminar case, but not before a sharp increase to about 12 times average upstream levels close to the trailing edge of the turbulent spot, at $x \approx 6D$. Even as turbulent breakdown continues to intensify and spread through the early deceleration phase, $P3$, ensemble-averaged axial shear stress levels remain low and negative in the turbulent region $4D \leqslant x \leqslant 6D$, dropping to values less than -5, lower than corresponding laminar levels.

Figure 24 indicates that WSS magnitudes in both stenosis models drop significantly after mid-deceleration, as the flow loses momentum. During phase $P4$, WSS at the throat drops to about 5 times average upstream levels and this continues through to minimum flow. In the immediate post-stenotic section, ensemble-averaged WSS profiles for the eccentric model rise to about 3 times average upstream values before falling below their laminar counterpart in the turbulent section between $x = 4D$ and $6D$. With relaminarization taking over during the late deceleration phase, shear levels in the region downstream of the throat remain low until they pick up when the flow starts to accelerate again. Throughout the deceleration phase, transition to turbulence in the case of the eccentric model results in the region beyond the turbulent section ($x \geqslant 7D$) attaining shear levels close to upstream levels. This is in sharp contrast with the axisymmetric model, where shear stresses in the entire post-stenotic region are lower than upstream levels during the deceleration part of the cycle.

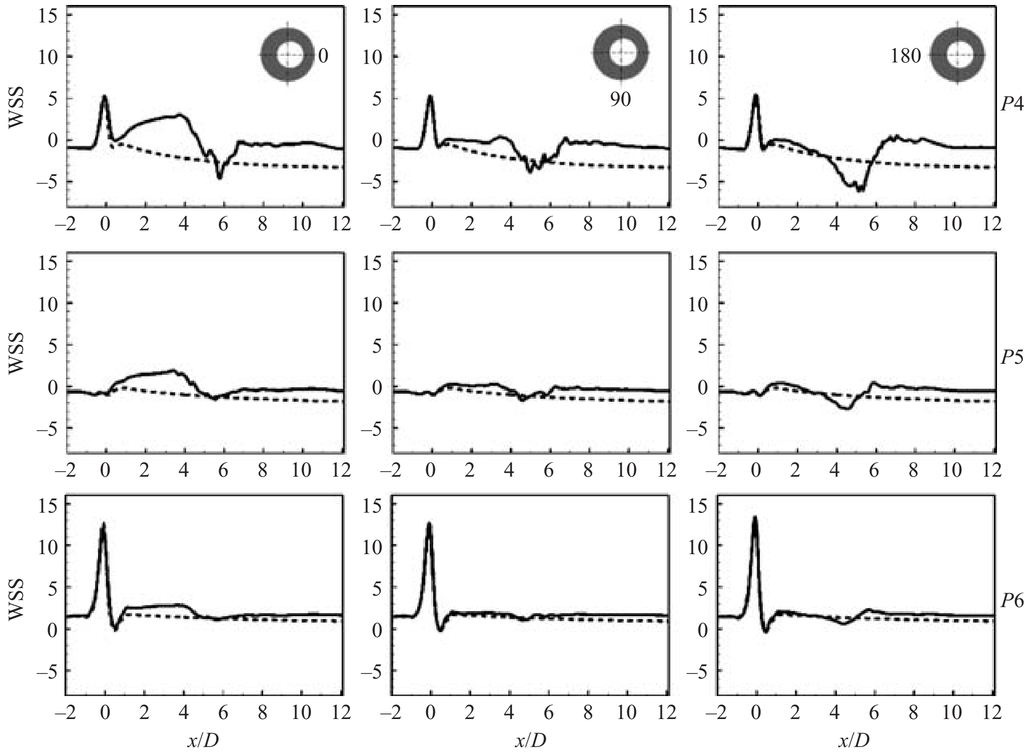

FIGURE 24. As figure 23 but during phases $P4$, $P5$ and $P6$.

WSS at the throat climbs up to more than 12 times average upstream levels by the early acceleration phase $P6$, while at the same time shear levels downstream of the eccentric stenosis get back closer to their laminar levels. By late acceleration, phase $P1$, shear levels throughout the eccentric model are almost identical to those in the axisymmetric model.

Figure 25 shows the instantaneous WSS distribution in the post-stenotic region between $x = 1D$ and $12D$ for the eccentric stenosis model, between phases $P2$ and $P5$. Corresponding plots at phases $P1$ and $P6$ have been omitted since they show no circumferential variation and are identical to the ensemble-averaged WSS profiles. At phase $P2$, peak inlet flow, the stenotic jet breakdown results in instantaneous axial shear levels rising and falling by more than a factor of 10 from time-averaged upstream levels. Both axial and circumferential gradients are significant between peak flow and the early deceleration phase $P3$. At $P3$, instantaneous shear stress magnitudes increase further, with maximum and minimum values of approximately 18 and −10, respectively, before dropping when the flow moves past mid-deceleration. Note the scale difference for the plot at phase $P3$. Shear levels at phases $P4$ and $P5$ indicate that the instantaneous WSS gradients in the turbulent region continue to drop as deceleration progresses, but levels remain mostly below zero during these times.

3.4. *Comparison with previous studies*

The pulsatile flow simulations were performed with flow parameters and geometry (axisymmetric) exactly the same as those used by Ahmed & Giddens (1984), and as seen in §3.1, the numerical results match very well with their laser Doppler

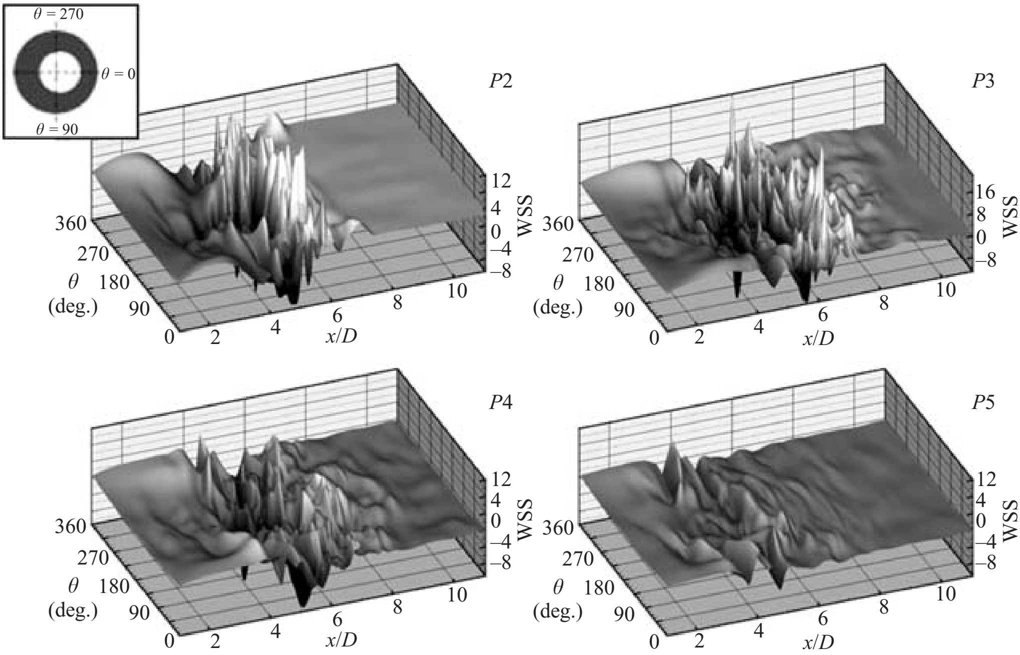

FIGURE 25. Sequence of instantaneous WSS in the post-stenotic region $1D \leqslant x \leqslant 12D$, highlighting the axial and circumferential distribution, for pulsatile flow through the 75 % eccentric stenosis. WSS levels have been normalized by the time-averaged WSS upstream of the stenosis. Note the scale difference for WSS during phase $P3$.

anemometry (LDA) measurements in the region immediately downstream of the stenosis. The numerical simulations through the axisymmetric model predict laminar flow downstream of the constriction, whereas there was evidence of disturbed flow in the experiments. The experimentalists reported stable flow during the early acceleration phase, followed by the formation of periodic coherent starting structures that were shed from the stenosis. Toward the end of acceleration, discrete-frequency velocity oscillations accompany this structure; and after peak flow, it was observed to break down into turbulence at $x \approx 6D$. This scenario closely resembles the one predicted by the numerics for the eccentric model under similar flow conditions, presented in § 3.2.

Numerical results for the axisymmetric model predict flow reattachment between $x = 7D$ and $8D$ under peak flow conditions, whereas in the experiments, reattachment was found to occur between $x = 5D$ and $6D$. However, simulations with the eccentric model showed reattachment occurring in exactly the same region as the experiments during peak flow, illustrated by phase-averaged velocity profiles in figure 8, indicating that transition to turbulence during this stage of the cycle promotes reattachment closer to the stenosis than in the corresponding laminar situation. This may explain the disagreement between the computed and experimental profiles at $x = 4D$ and $x = 6D$ in the near-wall region (figure 7). In contrast to its steady flow counterpart, pulsatile flow through both the axisymmetric and eccentric models has no permanent recirculation zone, with forward flow occurring across the entire vessel during the early acceleration phase, an observation also made by the experimentalists.

Earlier investigations by Cassanova & Giddens (1978) and Khalifa & Giddens (1981) characterized post-stenotic flow disturbances for pulsatile flow through an axisymmetric 75 % smooth stenosis model similar to the one used here. Their studies had minimum and peak Reynolds number (based on mean centreline inlet velocity) close to 500 and 2240, respectively, and Womersley parameters of $\alpha = 15$ in the former study and $\alpha = 8.4$ in the latter. These flow parameters are different to corresponding Reynolds numbers of 200 and 600 and $\alpha = 7.5$ employed in this study, but the post-stenotic flow behaviour is strikingly similar. Khalifa & Giddens (1981) identified three distinct types of flow disturbances in the downstream flow field: a coherent startup structure that formed at the beginning of each new cycle, shear layer oscillation due to flow separation, and turbulence. They reported that "turbulence appeared to rapidly interact with the starting structure, having evolved from a laminar oscillation which exists in the very near post-stenotic field". Centreline velocity waveforms from both studies qualitatively match our results for the eccentric case in figure 12, with evidence of the startup structure seen at immediate downstream stations, followed by high-frequency fluctuations after $x \approx 3D$ at peak flow, and during early deceleration. The disturbances start to dissipate toward the end of deceleration at all locations.

Another relevant comparison can be made with the flow visualization results of Ojha *et al.* (1989) who also studied pulsatile flow through a 75 % axisymmetric sharp-edged constriction with $\alpha = 7.5$ and mean and modulation Reynolds numbers (based on average cross-sectional inlet velocity) of 575 and 260, respectively. Even though these Reynolds numbers differ from the corresponding values of 300 and 347 used in this study, many of their findings are very similar to our results for the eccentric model. Their group observed that flow in the jet region, extending to $x \approx 3D$, appeared to be quite stable, with centreline velocities at these locations exhibiting a nearly sinusoidal variation. Kelvin–Helmholtz vortex roll-ups observed in this stable jet zone closely resemble those seen in the vorticity magnitude and streamwise velocity fluctuation contours illustrated in figure 9 and figure 21, respectively, during the late acceleration stage and at peak flow.

The experimental flow was in a transitional state throughout the cycle between $x = 3D$ and $4.5D$. Ojha *et al.* (1989) found that the reattachment location moved further downstream to $x \approx 4.5D$ close to minimum flow, where transition to turbulence was triggered by streamwise vortices generated earlier in the shear layer. Maximum turbulence occurred for about three vessel diameters after $x = 4.5D$, with the flow relaminarizing beyond $x = 7.5D$. These results match closely with the current eccentric study, in which streamwise vortices were found to play an important role in the transition process at $x \approx 4D$. The turbulent statistics presented in § 3.2.4 showed that turbulence intensity is indeed maximum between $x = 5D$ and $6D$ after peak flow, in the vicinity of the reattachment point, followed by relaminarization in the region beyond $x = 8D$. Complete flow relaminarization within the turbulent zone is not achieved because of insufficient time, and the r.m.s. profiles in figure 13 confirm the presence of small disturbances in this region during the acceleration phase, subsequently contributing to the transition process at peak flow. Ojha *et al.* (1989) labelled region $x/D > 7.5$ the 'relaminarization' zone. They also reported the presence of a permanent recirculation zone in the immediate downstream region as well as earlier transition to turbulence, in other words closer to the constriction than in the current simulations. These differences may be attributed to the higher mean Reynolds number employed in the experiments and their stenosis geometry.

Non-dimensional energy spectrum correlations by Cassanova & Giddens (1978) and Khalifa & Giddens (1981) showed broadband turbulent spectra after $x = 3D$, with a $-5/3$ slope over a broad range of frequencies, similar to those presented in § 3.2.5. The latter authors observed spectral peaks in the immediate vicinity of the constriction at a Strouhal number ($St = fd/u_p$) of 0.35, corresponding to passage of the startup structure through these locations. Mittal *et al.* (2003) conducted large-eddy simulations (LES) of pulsatile flow (with peak Reynolds number of 2000 and $\alpha = 8.6$) through a planar channel with a one-sided semicircular constriction and observed vortex shedding at a frequency of 0.45. The spectrum at $x = 3D$ in figure 18 shows a broad peak at $St \approx 0.39$, agreeing well with these studies. The presence of a $-10/3$ region in the spectra of stations in the turbulent zone also matches the findings by Lu *et al.* (1980), who computed spectra from *in vivo* velocity measurements in six calves in the vicinity of a surgically induced pulmonic stenosis.

In a quite recent stability analysis study of pulsatile flow through an axisymmetric stenosis model similar to that considered here, albeit at mean Reynolds number of 400 (based on average cross-sectional inlet velocity) and Womersley parameter of 15.9, Sherwin & Blackburn (2005) identified the nature of the instability in such flows as a tilting mechanism of the vortex ring generated during each pulsatile cycle at the front of the stenotic jet. This instability resulted in a rapid distortion of the vortex ring within a few diameters downstream of the stenosis and localized turbulent breakdown at $x \approx 6D$, followed by relaminarization in the far downstream region. Our observations that were made downstream of the eccentric stenosis model are consistent with this mechanism. While Sherwin & Blackburn (2005) introduced the instability by superimposing an unstable eigenmode on a stable base flow, the source of instability in this study was the eccentricity introduced at the stenosis throat, which tilts and distorts the vortex ring as it is ejected from the constriction. Similarly, geometric asymmetries or upstream noise may be responsible for transition to turbulence in the experiments by Ahmed & Giddens (1984). The simulations by Sherwin & Blackburn (2005) also demonstrated that the instability was subcritical, implying that turbulent flow can occur at lower Reynolds numbers than the critical value of 500. This phenomenon would explain the persistence of turbulence in the current simulations, in which the mean (cycle-averaged) Reynolds number was only 300 (based on average cross-sectional inlet velocity).

As in the steady flow study, and following the suggestion of a reviewer, we conducted a separate set of simulations for the axisymmetric stenosis that included the addition of a swirl-like perturbation to the inlet velocity profile. The streamwise velocity was unchanged from the Womersley profile, as defined in equation (2.1), but non-zero cross-stream inflow velocity components were specified such that the maximum amplitude of this perturbation was only 1 % of the mean centreline inlet velocity (u_c). The results obtained for this case confirmed that upstream disturbances can result in periodic, localized stenotic jet breakdown. We omit presenting these here since the computations were along the lines of the study by Sherwin & Blackburn (2005), with qualitatively similar results being obtained (different flow parameters did not allow more quantitative comparisons). Moreover, as mentioned in the first part of this study, our goal was to show that a quantifiable and perfectly replicable geometric perturbation in the form of a small stenosis eccentricity can result in post-stenotic transition to turbulence, even in the absence of upstream disturbances.

Ahmed & Giddens (1984) found that ensemble-averaged wall shear stress levels in the vicinity of flow reattachment, where intense turbulence occurred during part of the cycle, remained low. This matches our ensemble-averaged results for the eccentric model, in which axial shear levels were found to be mostly low and negative in the turbulent region $4D \leqslant x \leqslant 6D$, as shown in figures 23 and 24. However, Ojha *et al.* (1989) reported that instantaneous values in the turbulent section reached three times higher than upstream levels. Instantaneous axial wall shear stress results for the eccentric model indicated that magnitudes in fact increase by a factor of 12 from average upstream levels during peak inlet flow, when turbulent breakdown starts, and up to a factor of almost 18 during the early deceleration phase, when turbulence intensity peaks. While ensemble-averaged shear stresses help to provide an understanding of the wall stresses in an averaged sense, instantaneous realizations are clearly important to show the true spatial distribution of WSS.

4. Conclusions

Direct numerical simulations (DNS) have been used to study pulsatile flow through smoothly contoured 75 % stenosed vessels. Similar to the steady flow studies discussed in Part 1 of this study (Varghese *et al.* 2007), DNS predicted a completely laminar post-stenotic flow field in the case of the axisymmetric stenosis model. Comparing axial velocity profiles with previous experimental measurements, we found good agreement in the region immediately downstream of the stenosis, but this veered off in the vicinity of flow reattachment. Flow reattachment was found to occur further away from the stenosis in the case of the numerics, when compared to reattachment locations observed in the experiments, in which intermittent disturbed flow regions and turbulent breakdown were observed to occur around six diameters downstream from the throat ($x \approx 6D$).

The introduction of a stenosis eccentricity, that was 5 % of the main vessel diameter at the throat, resulted in jet breakdown and periodic, localized transition to turbulence. Analysis of the flow field at different times during the time-periodic cycle indicated that the early and mid-acceleration phases were relatively stable, with no turbulent activity in the post-stenotic region. However, during the late stages of acceleration, close to peak flow, the shear layer started to become unstable. The starting vortex formed during early acceleration, at the jet front as the fluid accelerated through the stenosis, started to break up into elongated streamwise structures, though the flow remained laminar at this point. Under peak inlet flow conditions, the streamwise vortices broke down, forming a turbulent spot between $x = 4D$ and $6D$, which continued to spread to about $x = 7D$ during early deceleration. Beyond $x = 7D$, the turbulent fluctuations and energy levels rapidly decayed and the flow almost completely reverted to its laminar character after $x = 11D$. Broadband velocity fluctuation spectra at axial stations within the spot confirmed turbulent flow, following the $-5/3$ energy cascade. By the advent of peak flow, a large recirculation region, continuously evolving in time and space, had formed downstream of the stenosis and was present through most of the deceleration phase. Turbulent breakdown during this time also resulted in early flow reattachment (relative to the axisymmetric case), occurring between $x \approx 6D$ and $7D$, similar to the experiments.

Turbulence intensity within the spot reduced as inlet flow lost its momentum, past the mid-deceleration stage and through to minimum flow, and the post-stenotic flow field began to relaminarize. This process continued into the early acceleration phase, during which time forward flow existed at all locations within the vessel. The absence of a permanent recirculation zone, in both the axisymmetric and eccentric models, is in agreement with experimental findings and in contrast to steady inlet flow observations. Residual fluctuations from the turbulent activity that occurred earlier in the cycle were at their lowest past the mid-acceleration point, though results indicate that there appears to be insufficient time for the post-stenotic section between the throat and $x \approx 9D$ to regain its normal laminar state, similar to the flow field upstream of the stenosis.

Wall shear stress levels at the stenosis throat were close to experimental measurements, rising to almost 75 times average upstream levels under peak flow conditions. However, in contrast to the axisymmetric case, WSS exhibited large spatial variations in the region $x > 1D$ for the eccentric model. In the averaged sense, shear levels in the turbulent section between $x = 4D$ and $6D$ remained low and negative during the turbulent breakdown process. However, instantaneous realizations indicated that magnitudes increase by a factor of almost 18 compared to time-averaged upstream levels, when turbulent energy peaked during early deceleration. Also, instantaneous axial and circumferential WSS gradients were significant after peak inlet flow and throughout the early deceleration phase, dropping away only as minimum inlet flow conditions approached. The region beyond the turbulent section experienced shear levels close to their upstream values, in contrast to the axisymmetric case, where stresses in the post-stenotic region were lower than upstream levels throughout deceleration. WSS in the region downstream of the eccentric stenosis were close to their laminar, axisymmetric counterparts through most of the acceleration phase.

Our study shows that a post-stenotic flow field rich in features such as recirculation, strong shear layers and periodic turbulent breakdown, affects wall shear stress through large spatial and temporal gradients, implicated in the progression of atherosclerotic disease (Ku 1997; Wootton & Ku 1999). The detailed representation and analysis of the flow field downstream of a clinically significant, albeit idealized, stenosis under physiologically realistic flow conditions (as defined by the Reynolds and Womersley numbers), complements earlier stenotic flow studies and serves as basis for understanding the complex flow fields that may arise in realistic arterial geometries. Comparison with earlier work suggests that the mechanics of turbulent breakdown, in terms of turbulent statistics, spectral correlations and the evolution of coherent structures downstream of the stenosis, is independent of the way in which it was brought about, be it a geometric perturbation such as a stenosis eccentricity or a perturbed inlet flow upstream of the stenosis, both of which are extremely relevant from the physiological point of view because real-life stenosed arteries are unlikely to exhibit any axisymmetry and nor is the upstream flow likely to resemble laminar, undisturbed, fully developed pipe flow. The DNS results presented in this study, along with those in Part 1, also provide a valuable database for validating turbulence models that can subsequently be employed to predict low-Reynolds-number biofluid flows, and particularly stenotic flows such as those considered here, to an acceptable level of accuracy.

This work was supported in part by the Mathematical, Information, and Computational Sciences Division subprogram of the office of Advanced Scientific Computing Research, Office of Science, US Department of Energy, under Contract DE-AC02-06CH11357.

REFERENCES

Ahmed, S. A. & Giddens, D. P. 1983 Velocity measurements in steady flow through axisymmetric stenoses at moderate Reynolds number. *J. Biomech.* **16**, 505–516.

Ahmed, S. A. & Giddens, D. P. 1984 Pulsatile poststenotic flow studies with laser Doppler anemometry. *J. Biomech.* **17**, 695–705.

Cassanova, R. A. & Giddens, D. P. 1978 Disorder distal to modeled stenoses in steady and pulsatile flow. *J. Biomech.* **11**, 441–453.

Eliahou, S., Tumin, A. & Wygnanski, I. 1998 Laminar-turbulent transition in Poiseuille pipe flow subjected to periodic perturbation emanating from the wall. *J. Fluid Mech.* **361**, 333–349.

Fischer, P. F., Kruse, G. & Loth, F. 2002 Spectral element methods for transitional flows in complex geometries. *J. Sci. Comput.* **17**, 81–98.

Han, G., Tumin, A. & Wygnanski, I. 2000 Laminar-turbulent transition in Poiseuille pipe flow subjected to periodic perturbation emanating from the wall. Part 2. Late stage of transition. *J. Fluid Mech.* **419**, 1–27.

Hinze, J. O. 1975 *Turbulence*. McGraw-Hill.

Jeong, J. & Hussain, F. 1995 On the identification of a vortex. *J. Fluid Mech.* **285**, 69–94.

Khalifa, A. M. A. & Giddens, D. P. 1981 Characterization and evolution of post-stenotic flow disturbances. *J. Biomech.* **14**, 279–296.

Kim, B. M. & Corcoran, W. H. 1974 Experimental measurements of turbulence spectra distal to stenoses. *J. Biomech.* **7**, 335–342.

Ku, D. N. 1997 Blood flow in arteries. *Annu. Rev. Fluid Mech.* **29**, 399–434.

Lieber, B. B. & Giddens, D. P. 1988 Apparent stresses in disturbed pulsatile flows. *J. Biomech.* **21**, 287–298.

Lieber, B. B. & Giddens, D. P. 1990 Post-stenotic core flow behavior in pulsatile flow and its effects on wall shear stress. *J. Biomech.* **23**, 597–605.

Lu, P. C., Gross, D. R. & Hwang, N. H. C. 1980 Intravascular pressure and velocity fluctuations in pulmonic arterial stenosis. *J. Biomech.* **13**, 291–300.

Mittal, R., Simmons, S. P. & Najjar, F. 2003 Numerical study of pulsatile flow in a constricted channel. *J. Fluid Mech.* **485**, 337–378.

Ojha, M., Cobbold, C., Johnston, K. & Hummel, R. 1989 Pulsatile flow through constricted tubes: An experimental investigation using photochromic tracer methods. *J. Fluid Mech.* **13**, 173–197.

Scotti, A. & Piomelli, U. 2001 Numerical simulation of pulsating turbulent channel flow. *Phys. Fluids* **13**, 1367–1384.

Shan, H., Ma, B., Zhang, Z. & Nieuwstadt, F. T. M. 1999 Direct numerical simulation of a puff and a slug in transitional cylindrical pipe flow. *J. Fluid Mech.* **387**, 39–60.

Sherwin, S. J. & Blackburn, H. M. 2005 Three-dimensional instabilities and transition of steady and pulsatile axisymmetric stenotic flows. *J. Fluid Mech.* **533**, 297–327.

Stettler, J. C. & Hussain, A. K. M. F. 1986 On transition of the pulsatile pipe flow. *J. Fluid Mech.* **170**, 169–197.

Stroud, J., Berger, S. & Saloner, D. 2000 Influence of stenosis morphology on flow through severely stenotic vessels: Implications for plaque rupture. *J. Biomech.* **33**, 443–455.

Tennekes, H. & Lumley, J. L. 1972 *A First Course in Turbulence*. MIT Press.

Varghese, S. S., Frankel, S. H. & Fischer, P. F. 2007 Direct numerical simulation of stenotic flows. Part 1. Steady flow. *J. Fluid Mech.* **582**, 253–280.

Waleffe, F. 1997 On self-sustaining process in shear flows. *Phys. Fluids* **9**, 883–900.

Welch, P. D. 1967 The use of fast Fourier transform for the estimation of power spectra: A method based on time averaging over short modified periodograms. *IEEE Trans. Audio Electroacoust.* AU **15**, 70–73.

Wilcox, D. 1993 *Turbulence Modeling for CFD*. La Cañada, California, CA: DCW Industries.

Womersley, J. R. 1955 Method for the calculation of velocity, rate of flow and viscous drag in arteries when the pressure gradient is known. *J. Physiol.* **127**, 553–563.

Wootton, D. M. & Ku, D. N. 1999 Fluid mechanics of vascular systems, diseases, and thrombosis. *Annu. Rev. Biomed. Engng* **1**, 299–329.

Wygnanski, I. J. & Champagne, F. H. 1973 On transition in a pipe. Part 1. The origin of puffs and slugs and the flow in a turbulent slug. *J. Fluid Mech.* **59**, 281–335.

Wygnanski, I. J., Sokolov, M. & Friedman, D. 1975 On transition in a pipe. Part 2. The equilibrium puff. *J. Fluid Mech.* **69**, 283–304.